

UNIVERSITÀ DEGLI STUDI DI PADOVA

DIPARTIMENTO DI FISICA E ASTRONOMIA

CORSO DI LAUREA MAGISTRALE IN
ASTRONOMIA

DEMOGRAPHY OF
BINARY NEUTRON STARS:
THE IMPACT OF NATAL KICKS AND
ELECTRON-CAPTURE SUPERNOVAE

RELATORE

Prof. Michela Mapelli

CORRELATORI

Dr. Nicola Giacobbo
Dr. Giuliano Iorio

LAUREANDO

Nicola Gaspari

ANNO ACCADEMICO 2019/2020

Alla mia famiglia

Contents

1	INTRODUCTION	1
2	ISOLATED NEUTRON STARS	7
2.1	Stellar evolution of the progenitors	7
2.1.1	General features	7
2.1.2	Main sequence	10
2.1.3	Post-main-sequence phases	11
2.1.4	Late evolution	13
2.2	Formation of the compact remnant	16
2.2.1	Core-collapse supernovae	16
2.2.2	Electron-capture supernovae	17
2.3	Birth properties of neutron stars	18
2.3.1	Mass	18
2.3.2	Natal kick	20
2.3.3	Spin and magnetic field	21
3	BINARY NEUTRON STARS	25
3.1	Stellar evolution of binary stars	25
3.1.1	Grounding ansatz	25
3.1.2	Mass transfer	25
3.1.3	Common envelope	30
3.1.4	Kicks	31
3.1.5	Gravitational waves	33
3.1.6	Other processes	35
3.2	Formation scenarios for binary neutron stars	36
4	SYNTHESIS OF STELLAR POPULATIONS	39
4.1	The SEVN code	39
4.1.1	Overview	39
4.1.2	Updates	41
4.2	Initial conditions for population synthesis	42
4.2.1	Masses	42
4.2.2	Orbital parameters	43
5	RESULTS	47
5.1	ECSNe and natal kicks in binary stars	47
5.2	Mass distribution of BNS progenitors	49
5.3	BNSs in single stellar populations	51
5.4	BNSs from continuous star formation	52
5.5	Merger rate	55
6	SUMMARY AND CONCLUSIONS	59
	BIBLIOGRAPHY	63

CHAPTER 1

Introduction

Neutron stars (NSs) are collapsed stellar cores that owe their existence to the death of massive stars. They weight slightly more than the Sun but are only ~ 10 kilometers in radius, which is why they are so dense to resemble more an atomic nucleus than a regular star. They host among the strongest magnetic fields in the observable Universe, and their gravitational pull is second only to that of a black hole. In fact, if a neutron star gets any denser it will turn into one of them. Such extreme physical conditions make these stellar corpses not only a probe into the life of a star but also a unique laboratory for several fields of physics.

Since their prediction (Baade and Zwicky 1934)¹ and the emergence of the first models (Oppenheimer and Volkoff 1939), neutron stars have been unambiguously linked to a plethora of different observations, being found alone (e.g. Hewish et al. 1968), in couple with ordinary stars (e.g. Giacconi et al. 1962), or even with other neutron stars (e.g. Hulse and Taylor 1975). Due to the extreme compactness of these objects, their motion is able to perturb the fabric of spacetime and produce ripples in it. The first strong evidence of these perturbations, also known as gravitational waves (GWs), was indeed provided by the Hulse-Taylor binary neutron star (BNS), whose orbit shrinks according to Einstein's general relativity. In such binaries, GWs are produced by the orbital motion of the two bodies and their emission extracts energy from the binary, damping the motion and shrinking the orbit. As the emission increases with the orbit getting smaller, the orbital damping eventually gets so strong to doom the binary to a coalescence (Peters 1964).

Other than being recognized as prime sources of GWs, BNS mergers have long been thought to give rise to various electromagnetic counterparts, such as short gamma-ray bursts (sGRB, for a review see Berger 2014) or kilonovae (for a review see Metzger 2019). The observation of these phenomena altogether has always been challenging due to their elusive nature, and not a single BNS merger has ever been clearly identified until three years ago. On the 17th August 2017, the interferometers of LIGO and Virgo detected a GW signal with a chirp compatible to that of a merging BNS. The GW event named GW170817 ended at 12:41:04.4 UTC and its ~ 100 s long signal had the highest signal-to-noise ratio ever observed, making it the longest and loudest yet recorded (Abbott et al. 2017a). Less than 2 s after GW170817 end, both the *Fermi Gamma-ray Space Telescope* and *INTEGRAL* detected a sGRB coming from a region overlapping the GW event location. The dispatch of reports on these almost-simultaneous detections immediately unleashed a fleet of telescopes on the hunt for electromagnetic counterparts, leading to the identification of a new optical transient 12 hours later. The transient, named AT 2017gfo and localized in the lenticular galaxy NGC 4993, has shown a dimming spectrum with broad lines likely due to neutron-rich heavy elements, consistent with the kilonova from a BNS merger. All these coincident detections, namely gravitational wave, short gamma-ray burst, kilonova, and subsequent X-ray and radio counterparts, have

¹It is possible that the original intuition came from Landau (Yakovlev et al. 2013).

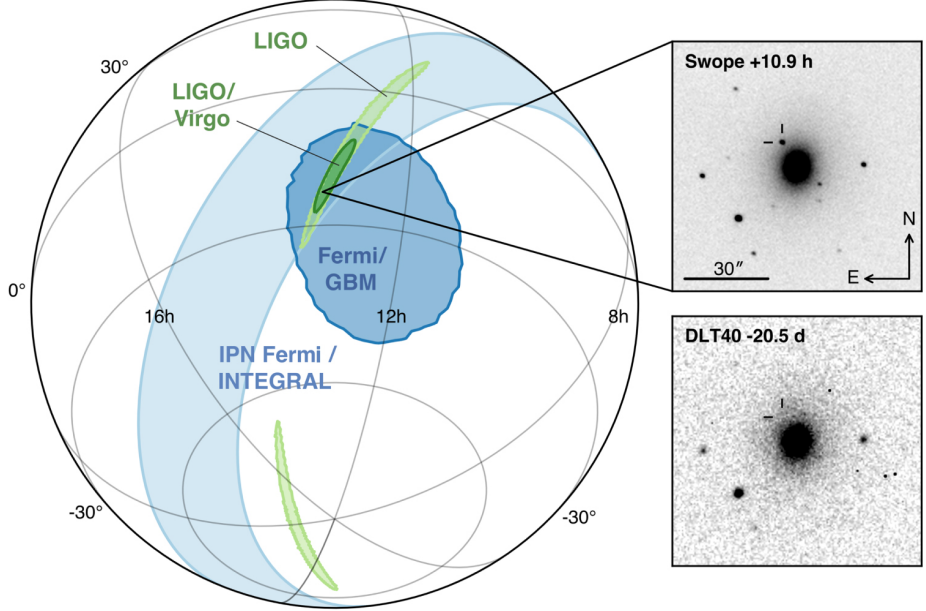


Figure 1. Localization of the gravitational-wave, gamma-ray, and optical signals coming from the BNS merger of 17th August 2017. The main panel shows initial gravitational-wave 90% areas in green (with and without Virgo) and gamma-rays in blue (the InterPlanetary Network triangulation from the time delay between *Fermi* and *INTEGRAL*, and the *Fermi* Gamma-ray Burst Monitor localization). The inset shows the location of the optical counterpart (the top panel was taken 10.9 hours after merger with the Swope Telescope, the lower panel is a pre-merger reference without the transient from the DLT40 Survey). Figure and caption adapted from Abbott et al. (2017b).

now clearly identified as the different facets of the first direct observation of a binary neutron star merger (Abbott et al. 2017b).

The direct observation of BNS mergers contributes in a substantial way to our knowledge of BNSs and the topics they are connected to (Barack et al. 2019). It is impactful already with one of the most direct questions it answers, that is “how many mergers there are per unit volume and unit time”, or in short “at which rate BNSs merge”. The merger rate is known to deeply depend on the progenitors’ evolution, to such an extent that theoretical predictions of the rate can vary by two orders of magnitude (Abadie et al. 2010; Dominik et al. 2012). The main observational estimate before GW170817 was extrapolated from the properties of Galactic BNSs (e.g. Kalogera et al. 2004), but its uncertainties were too high to constrain the predictions. Today we can infer a direct estimate from the GW observations, which is still uncertain due to low statistics ($290\text{--}2810 \text{ Gpc}^{-3} \text{ yr}^{-1}$, 90% credible interval from Abbott et al. 2020) but will get more precise as the observation time increase. With the narrowing of the merger rate uncertainties we can expect to rule out inconsistent models, and this motivates a comprehensive study of the evolutionary processes behind the BNS demography (e.g. Belczynski et al. 2018).

This thesis presents a study on the statistical properties of isolated BNS populations, by means of stellar population synthesis. The work focuses on the impact of two critical processes, namely electron-capture supernovae (ECSNe)

and natal kicks. The former is a putative NS formation channel involving stars that are not massive enough to undergo classic iron core-collapse supernovae (CCSNe). The latter is the recoil given to the NS by an asymmetric SN explosion, which shapes the orbit, regulates binary disruptions, and is a long-standing matter of debate.

The study employs the population-synthesis code SEVN, which has already been used to study single and binary isolated BHs (Spera et al. 2015; Spera and Mapelli 2017; Spera et al. 2019). Together with SEVN, thi thesis employed a novel Python code that generates realistic initial conditions for binary systems, based on observational constraints. Most of the work behind this thesis consisted in developing and testing these codes, with the aim to simulate realistic BNSs.

The thesis is structured as follows. Chapter 2 summarizes the evolutionary path that leads a star to become a NS and provides a brief survey of the NS's birth properties, so that a basic framework for the formation of single NSs is established. Chapter 3 summarizes the main evolutionary processes of binary stellar systems aside single stellar evolution, and outlines two standard formation scenarios for merging BNSs. Chapter 4 reviews the implementation in the SEVN code of the theoretical framework given above, together with physically-motivated initial conditions for population synthesis. Chapter 5 exposes and analyzes a set of synthetic populations simulated with the SEVN code, focusing on the demography of BNSs and their progenitors. Chapter 6 gives a final summary, together with possible future development.



Figure 2. The kilonova AT 2017gfo from the BNS merger of 17th August 2017, and its host galaxy NGC 4993. The transient faded really quick in few days after its detection, as shown by the insets. The host galaxy is a lenticular galaxy located 42.5 Mpc away from the Milky Way, in the Hydra constellation. It shows shell-like features in the outer stellar component, and edge-on spiral-like dust lanes around the center, suggesting a turbulent past. This image was taken with the WFC3 instrument on the *Hubble Space Telescope* at optical/infrared wavelengths. Credit: NASA and ESA. Acknowledgment: N. Tanvir (U. Leicester), A. Levan (U. Warwick), and A. Fruchter and O. Fox (STScI)

CHAPTER 2

Isolated neutron stars

This Chapter presents a summary of the current theory of stellar evolution, focusing on the path taken by isolated massive stars ($M \gtrsim 8 M_{\odot}$) to become NSs. A brief survey of NS's birth properties is also presented.

Part of this Chapter is based on the book *Stellar Structure and Evolution* from Kippenhahn et al. (2012) (hereafter abbreviated to KIP 2012), and follows its notation. Further details on single stellar evolution have been collected from Chiosi (1998) and Woosley et al. (2002). The Section on NSs is based on the lecture notes of Turolla (2019) on relativistic astrophysics.

2.1. STELLAR EVOLUTION OF THE PROGENITORS

2.1.1 General features

Nondegenerate stars (hereafter simply stars) are giant spheres of glowing plasma that populate the Universe and live on a precarious equilibrium. On one side there is their own gravity, which steadily works to squeeze them, while on the other side there is their internal pressure, which pushes against gravity¹. The balance between the two drives the stellar evolution, and to understand how it works let us start from noticing that almost all stars must evolve in near-perfect hydrostatic equilibrium.

If we suppose that hydrostatic equilibrium does not hold, then the stellar structure should change on a free-fall timescale

$$\tau_{\text{hydro}} \approx \sqrt{\frac{R^3}{GM}} \quad (2.1)$$

Hydrostatic equilibrium
and virial theorem

where G is the gravitational constant, while R and M are the radius and the mass of the star. For a solar mass star, this timescale ranges from roughly half an hour for the Sun ($R = 1 R_{\odot}$) to 18 days for a red giant ($R = 100 R_{\odot}$). Hence, if stars evolve far from hydrostatic equilibrium we should see collapses or explosions quite often, but since this is not observed we can safely assume they live in a near-perfect hydrostatic equilibrium² (KIP 2012, §2.4).

The condition of hydrostatic equilibrium in a spherically-symmetric fluid body can be expressed equaling the pressure gradient to the gravitational force

$$\frac{dP}{dm} = -\frac{Gm}{4\pi r^4}, \quad (2.2)$$

where P is the pressure and

$$m = \int_0^r 4\pi \tilde{r}^2 \rho d\tilde{r} \quad (2.3)$$

¹For the sake of conciseness, the following exposition assumes that stars are non-rotating and have negligible magnetic fields.

²It is necessary to mention that there exist several classes of variable stars, which show periodic changes on a timescale around τ_{hydro} . This behavior can be explained by small oscillations about the hydrostatic equilibrium.

is the mass coordinate, a lagrangian generalized coordinate that identifies the radius r enclosing the mass m . Under the simplifying assumption that the star is made of an ideal monoatomic gas, the integration over the whole star's mass M of (2.2) gives

$$E_{\text{in}} = -\frac{1}{2}E_{\text{gr}} \quad (2.4)$$

where the left hand side

$$E_{\text{in}} = \int_0^M \frac{P}{\rho} dm \quad (2.5)$$

is the internal energy, and the right hand side

$$E_{\text{gr}} = - \int_0^M \frac{Gm}{r} dm \quad (2.6)$$

is the gravitational energy (KIP 2012, §3.1).

Equation (2.4) is known as the virial theorem for an ideal gas, and it gives us a great insight into the stellar evolution. Let us define the total energy of a star as

$$E = E_{\text{in}} + E_{\text{gr}} < 0 , \quad (2.7)$$

where we have neglected the kinetic energy from the bulk motion of the gas since it is in hydrostatic equilibrium. As the star radiates energy from its surface, if we assume that there is no internal source supplying the energy radiated then it must be supplied by E , that is to say the star's luminosity L must be the opposite of the time derivative of E

$$L = -\dot{E} > 0 . \quad (2.8)$$

Expressing \dot{E} by means of (2.3)

$$\dot{E} = -\dot{E}_{\text{in}} = \frac{1}{2}\dot{E}_{\text{gr}} , \quad (2.9)$$

we can see the implications of the virial theorem for a radiating star without an internal energy source: as energy leaves its surface, the star contracts

$$\dot{E}_{\text{gr}} = -2L < 0 \quad (2.10)$$

and gets hotter

$$\dot{E}_{\text{in}} = L > 0 . \quad (2.11)$$

In other words, stars are systems with a negative heat capacity.

The main effect of the heating contraction predicted by the virial theorem is that eventually the stellar interior reaches such high temperatures and densities to start nuclear fusion reactions. These reactions release energy and act as an internal energy source, supplying the energy lost from the surface as radiation and neutrinos. Referring to the energy produced by nuclear fusion as E_{nuc} , this means

$$L = -\dot{E}_{\text{nuc}}, \quad (2.12)$$

and implies that the total energy is not consumed and remains constant in time

$$\dot{E} = \dot{E}_{\text{in}} = \dot{E}_{\text{gr}} = 0 . \quad (2.13)$$

In such stationary state the star cannot expand, contract, or change its temperature, and is said to be in thermal equilibrium.

Nuclear fusion is said to burn fuel into ash, the fuel being nuclides and the ash being the fusion products, and each element burns at a different temperature, which increase with the atomic number. The energy generation rate per unit mass of a nuclear fusion reaction can be approximated as

$$\varepsilon_{ij} = \varepsilon_0 X_i X_j \rho T^\nu , \quad (2.14)$$

where ε_0 and ν are constants characterizing for the reaction, X_i is the mass fraction of the nuclear species i , ρ is the density, and T is the temperature (KIP 2012, §18.3). The energy production rate couples with the negative heat capacity of the star, creating a thermostatic effect that account for the stability of the thermal equilibrium. If we assume that at some point $L_{\text{nuc}} > L$, then we will have $\dot{E} > 0$, and the star will react to keep the hydrostatic equilibrium. By the virial theorem, this will lead to an expansion and a cooling of the star, which will last until ε_{ij} drops enough to get $L_{\text{nuc}} = L$.

As the fusion takes place, fuel is consumed and ashes are piled up, until the fuel gets exhausted and the nuclear burning stop. The shutdown of the energy source brings the star to a new heating contraction, which eventually raises the central temperature until a heavier element is ignited. The star can undergo several cycles of contraction and nuclear burning, each one grows a new smaller core made out of the nuclear ashes, and will end up shaping the stellar interior in an onion-like structure.

The brief stellar evolution laid out so far is characterized by three timescales, the first of which is τ_{hydro} . The second timescale is related to the deviations from thermal equilibrium, such as the shutdown of an internal energy source or the subsequent heating contraction. It can be estimated by the Kelvin-Helmholtz timescale

$$\tau_{\text{KH}} = \frac{E_{\text{in}}}{L} \approx \frac{|E_{\text{gr}}|}{L} \approx \frac{\mathcal{G}M^2}{2R} , \quad (2.15)$$

which is the time needed by the star to radiate almost all of its internal energy. The third timescale is given by the duration of the nuclear burning, which also dictates the pace at which the chemical evolution unfolds. Since the nuclear burning takes place in thermal equilibrium, so $L = \dot{E}_{\text{nuc}}$, the nuclear timescale can be estimated as

$$\tau_{\text{nuc}} = \frac{E_{\text{nuc}}}{L} = \frac{\eta M_{\text{fuel}} c^2}{L} \quad (2.16)$$

where M_{fuel} is the initial rest mass of nuclear fuel, and η is the fraction of the fuel rest mass that is converted into energy by nuclear fusion.

For a star like the Sun, the Kelvin-Helmholtz timescale is around 10^9 yr, while the nuclear timescale for hydrogen burning is around 10^{10} yr, so

$$\tau_{\text{hydro}} \ll \tau_{\text{KH}} \ll \tau_{\text{nuc}} , \quad (2.17)$$

and in general this trend holds for all the stars that burn hydrogen or helium in the core (KIP 2012, §4.6).

With this general picture in mind, the life of a star can be summarized as the very short collapse of a gas cloud into a compact object (or even nothing), stalled by very long periods of nuclear burning.

Evolutionary timescales

2.1.2 Main sequence

A star is said to be born when hydrogen burning (H-burning) is ignited at its core and the energy produced fully supplies the energy lost as luminosity. We refer to the core hydrogen-burning phase as the main sequence (MS) of a star, with the starting point being the zero-age main sequence (ZAMS). The MS is the longest evolutionary phase, as a star spends more than 90% of their life burning hydrogen in the core, and thus it is the most common phase in which stars are observed (Chiosi 1998).

Prior to the MS, the protostar evolves through a series of stages that last between τ_{hydro} and τ_{KH} . As the star settles on the ZAMS, the stellar structure quickly adjust to hydrostatic and thermal equilibrium on a time τ_{KH} , and is almost uniquely determined by mass and composition (KIP 2012, §27-28).

Main sequence lifetime

Since stars on the ZAMS share conditions as near-homogeneity and total equilibrium, they show some degree of self-similarity. In particular, if they have the same relative mass distribution³, we can derive scaling relations involving several stellar parameters, such as mass, radius and luminosity, which are called homology relations (KIP 2012, §20). A classic homology relation that applies to ZAMS stars is the $M-L$ relation for a homogeneous radiative star with constant opacity and an ideal-gas equation of state, that is

$$L \propto \mu^4 M^3 \quad (2.18)$$

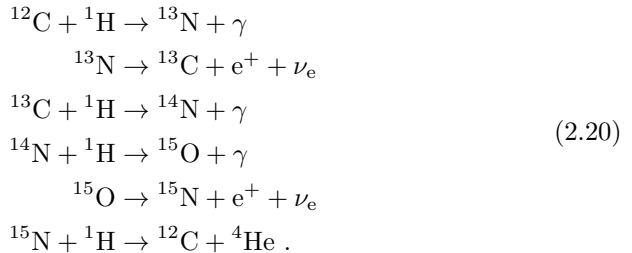
where μ is the mean molecular weight. If we plug this relation in (2.14), and make the very rough approximation that all the MS stars burns approximately the same mass fraction of helium, we get

$$\tau_{\text{nuc},\text{H}} \propto \frac{M}{L} \propto M^{-2} \quad (2.19)$$

which means that the MS lifetime is shorter at higher masses. Typical values for the MS lenght range from $\sim 10^{10}$ yr for a $1 M_\odot$ star, to $\sim 10^6$ yr for a $100 M_\odot$ star (KIP 2012, §30.3).

Core hydrogen-burning

During the main sequence, massive stars burn hydrogen into helium via the CNO cycle (KIP 2012, §18.5), whose main reaction chain is



The nuclear burning releases enough energy to break the Schwarzschild criterion (KIP 2012, §6.1) and to develope a convective core, while the radiative transport remains active in the surrounding envelope. As helium builds up in the core and radiation diffuses towards the surface, the stellar structure slowly changes leading to an increase in radius and luminosity, and a decrease in the effective temperature

³By relative mass distribution we mean a function mapping r/R to m/M .

(see Figure 3 and 4). Also, the central temperature T_c and the central density ρ_c increase during the MS, constrained by the hydrostatic equilibrium⁴ to scale as

$$T_c \propto M^{\frac{2}{3}} \rho_c^{\frac{1}{3}}. \quad (2.21)$$

Major complications affect this scenario if the star is rather massive. As the size of the core increases with ZAMS mass, it can reach the point where it becomes a relevant portion of the stellar structure. Since the core of massive stars is convective, this enhances the impact of complex features such as semiconvection and overshooting. Moreover, at higher masses the luminosity can rise to such an extent that radiation pressure lifts the outermost layers of the star. Between ~ 25 and ~ 50 M_\odot , the effect of the wind during the MS is to reduce the stellar mass and to inhibit the growth of the helium core. Above ~ 50 M_\odot , the wind became so strong that the whole outer envelope is ejected before the MS ends, leaving a bare helium core. This drastically changes the evolution of the star, and lead to the so-called Wolf-Rayet stars (Chiosi 1998; Woosley et al. 2002).

Convection and mass loss

2.1.3 Post-main-sequence phases

When the core is depleted in hydrogen, the nuclear burning suddenly turns off from the center to the outside, leaving a H-burning shell sitting above an inert helium core. Due to the thermostatic effect of nuclear burning, the presence of the shell H-burning couples the dynamical behavior of what is above and below it, acting as a mirror. Whenever the core contract the envelope expands, and vice versa. This effect takes place every time a burning shell is present and is called the mirror principle.

Hertzsprung gap

The core, without an energy source, starts to contract and heat on a time τ_{KH} , returning radiative. At the same time, the envelope expands and cools down. This change of the envelope causes a sudden drop in the effective temperature and starts to increase the envelope opacity, setting convection in motion. Doing so, the star departs from the MS and jumps towards the Hayashi line, which is the evolutionary track on the Hertzsprung-Russell (HR) diagram that the star would follow if it was completely convective. This phase is called the Hertzsprung gap since the transition is so quick that few stars are found in this phase (KIP 2012, §31.1).

When the star reaches the Hayashi line, it starts to climb the track as a red giant until the helium-burning (He-burning) is ignited in the core. The nuclear burning halts the core contraction and makes it convective again, while the shell H-burning makes the envelope contract due to the mirror principle. In this process, the convective envelope is forced to recede and a radiative one takes its place, while the star descends the Hayashi line and possibly increase its effective temperature, making the so-called blue loop on the HR diagram (Chiosi 1998; KIP 2012, §6.1). During this whole phase, helium is first being burned by the so-called triple- α process



Red giant branch and core helium-burning

and then, when enough ${}^{12}\text{C}$ is created, by



⁴This scaling relation can also be derived as an homology relation.

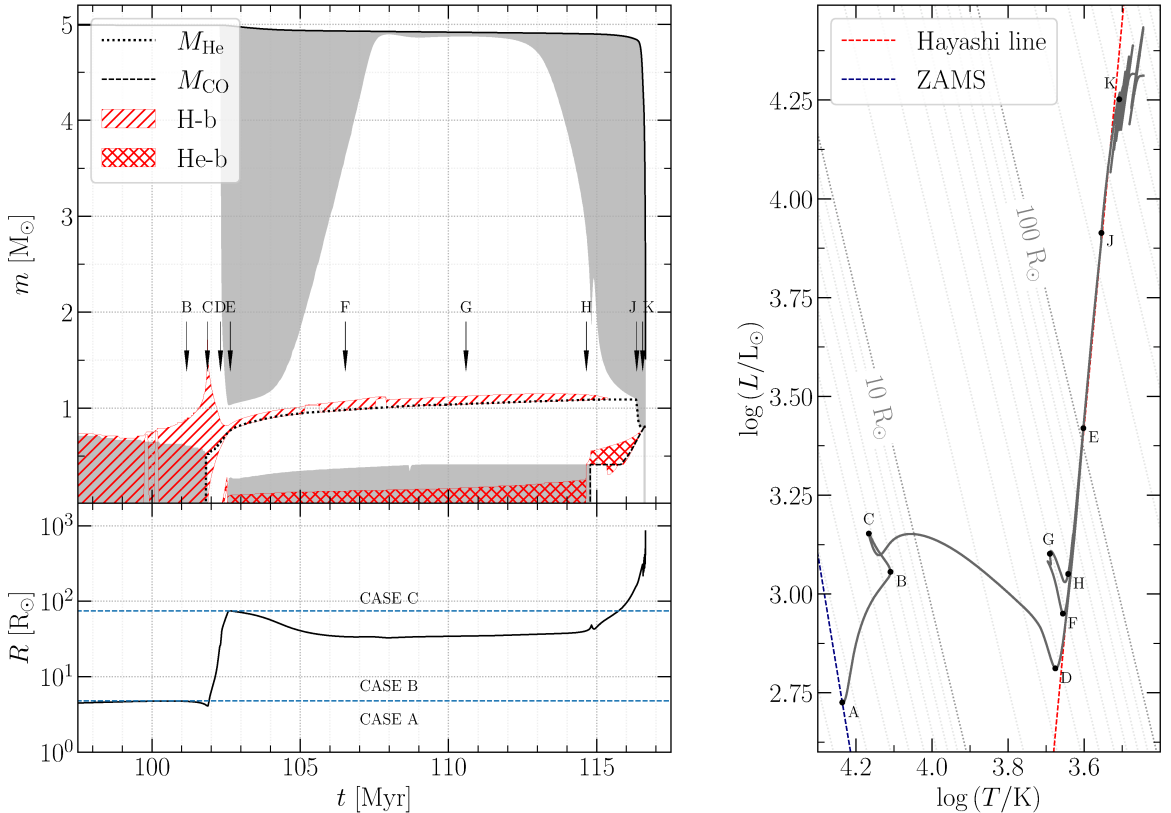


Figure 3. Left: Kippenhahn diagram of a $5 M_{\odot}$ star with metallicity $Z = 0.02$ (above), and evolution of its radius (below). In the Kippenhahn diagram are shown: the boundaries of the He and CO cores (resp. M_{He} and M_{CO}), the convective regions (in grey), the H-burning and He-burning regions (resp. H-b and He-b). In the radius diagram there are the interval in which either RLO Case A, B or C can be triggered (see Section 3.1.2). Right: HR diagram of the same star. There are shown: the ZAMS, the Hayashi line, and several evolutionary keypoints. In particular, the main sequence goes from A to c, the Hertzsprung gap from c to d, the first giant branch phase from d to e, the core He-burning from e to h, and the asymptotic giant branch phase from h onwards, with the second dredge-up at j and the beginning of the thermally-pulsating phase at k.

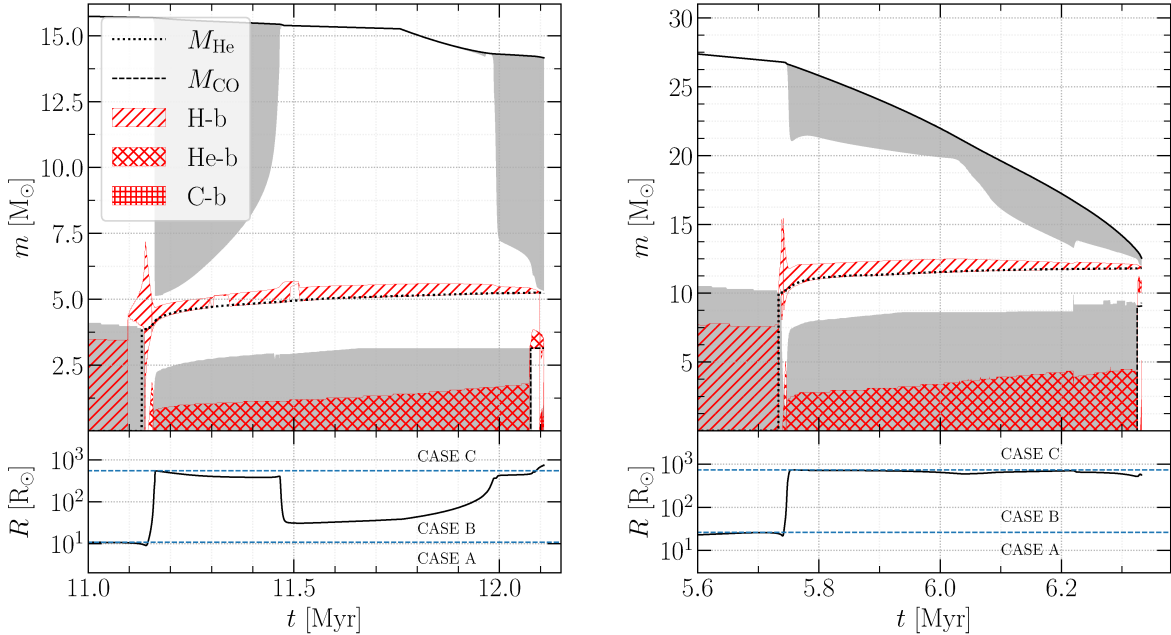


Figure 4. Kippenhahn diagram and radius evolution of a 16 M_\odot star (left) and a 30 M_\odot star (right), both with $Z = 0.02$. The C-burning regions (C-b) are so short lived that they are almost undistinguishable.

While the carbon-oxygen (CO) core is being created, the H-burning shell is still active and continues to grow the helium shell.

As before, the scenario holds plain only for the lighter massive stars. Assuming for reference the solar metallicity, stars with ZAMS mass above $\sim 15 \text{ M}_\odot$ begin to evolve differently because of convection and mass loss. In the range from ~ 15 to $\sim 25 \text{ M}_\odot$, the envelope is partially lifted by winds, but stars still cross the Hertzsprung gap and climb the red giant branch. At increasing masses the blue loop gets suppressed and the core He-burning is spent near the Hayashi line, producing what are known as a red supergiants. In the range from ~ 25 to $\sim 50 \text{ M}_\odot$, stars can lose the hydrogen envelope while red supergiants and likely become Wolf-Rayet stars, while stars above $\sim 50 \text{ M}_\odot$ become naked helium cores already during the MS (Chiosi 1998; Woosley et al. 2002; KIP 2012, §32).

2.1.4 Late evolution

Once the core is depleted in helium, the He-burning moves in a shell above the core. Devoid of its energy source, the core starts to contract and heat again, and its fate mainly depends on whether its mass is above or below the critical limit

$$M_{\text{Ch}} = 5.84 \mu_e^{-2} \text{ M}_\odot \quad (2.24)$$

known as Chandrasekhar mass, where μ_e is the mean molecular weight per free electron (KIP 2012, §19.7). This limit concerns cores that are contracting without an internal energy source, and separate those who develop degenerate electrons from those who do not. If the core mass cannot grow above the Chandrasekhar mass, then at some point during the contraction the electrons

Chandrasekhar mass

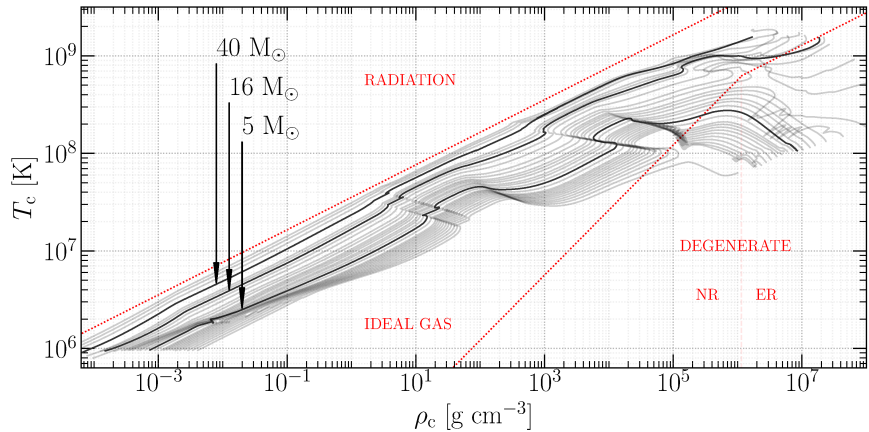


Figure 5. Evolution of T_c and ρ_c in stars with masses between 2 and $60 M_\odot$, with $Z = 0.02$. The tracks of stars in Figures 3 and 4 are highlighted. Stars are evolved until they reach TP-AGB phase or the end of C-burning. The diagram is splitted according to the leading pressure term (estimated in MS), which can be radiation, matter (approximated to an ideal gas), or degenerate electrons (either non-relativistic and extremely-relativistic). Note that tracks evolve closely to what is prescribed by (2.21). The major deviations appear when a new nuclear burning cycle is initiated (the track turn around in a “C” shape), when neutrino cooling kicks in at $T_c \sim 10^9$ K, and when the core becomes degenerate.

become degenerate, and the degeneracy pressure prevents the core to contract further. On the other side, if the core mass grows above the Chandrasekhar mass then electron degeneracy is never reached, and the contraction lasts until the ignition of carbon burning. This criterion is also used to classify stars, the former being called intermediate-mass stars and the later massive stars. Halfway between these two classes lies a third evolutionary path, which is undertaken when the CO core gets very near to the Chandrasekhar mass but the electron degeneracy is not the last stage for the core (KIP 2012, §35.2).

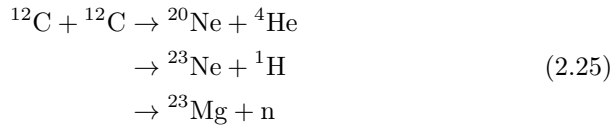
In intermediate-mass stars, the stellar structure after the core He-burning is composed of an inert CO core, a He-rich shell, and an outer envelope. At the beginning, the He-rich shell has shell He-burning at its bottom and shell H-burning at its top. As the the contraction of the core sets in, the He-burning induces an expansion of the He-rich layer due to the mirror principle, which then cools down and extinguishes the H-burning at its top. With the only one burning shell, the expansion involve also the outer envelope, leading the convection to extend from the surface toward the stellar interior. The growing convective region gets the star to climb again the Hayashi line, engaging a phase called early asymptotic giant branch (E-AGB) since it asymptotically approaches the path of the first giant branch. As the shell He-burning continues to increase the CO mass, the electrons in the core become fully degenerate and their degeneracy pressure halts the core contraction (KIP 2012, §34.1).

As the convective envelope reaches deeper layers, it eventually penetrates down in the He-rich shell. During this event, called second dredge-up⁵, the convective envelope brings heavy elements toward the surface, and new hydrogen in the

⁵The first dredge-up can occur during the first giant branch.

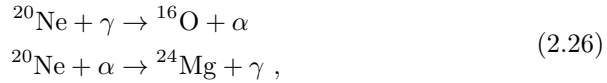
regions belonging to the He-rich shell. As the bottom of the convective envelope gets closer to the He-burning shell, the former starts to heat and eventually reignites shell H-burning. The configuration in which two shells are burning at the same time is thermally unstable and brings the star in a phase called thermally pulsating asymptotic giant branch (TP-AGB). In this phase the shell He-burning is normally quenched, while the shell H-burning goes on and adds helium to the intershell region. Periodically the shell He-burning reignites in a short-lived flash of increasing luminosity (they exceed $\sim 10^7 L_\odot$ in few cycles), growing the CO core and quenching the shell H-burning. The violent periodic variation in luminosity induces stellar pulsations and a dust-driven wind, which peels off the degenerate core until the star becomes a white dwarf surrounded by a planetary nebula (KIP 2012, §34.3).

The evolution of massive stars deviates from that of intermediate-mass star near the end of E-AGB, if the mass loss has not already removed part of the envelope. The main difference between the two path is that massive stars never reach electron degeneracy in the core. Therefore, after the CO core starts to contract, it goes on until the carbon-burning (C-burning) is ignited. The nuclear burning reaction has several branches, the main ones being

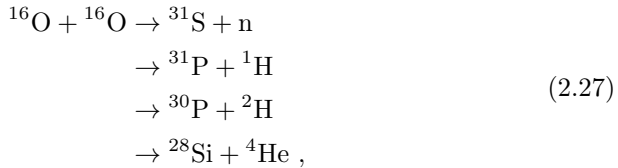


Nuclear burning in massive stars

and when the carbon gets exhausted, the cycle of contraction and burning repeats. The star goes through neon burning



then oxygen burning



and finally silicon burning, which is a long chain of photodisintegration and α -capture that produces iron. Note that neon and silicon burnings rely on photodisintegration rather than nuclear fusion (Woosley et al. 2002).

The whole late evolution of massive stars is characterized by a complex network of side reactions that results in a rich nucleosynthesis. The evolution ends with the production of iron because elements beyond iron have decreasing binding energy, and so their fusion cannot provide energy to support the core contraction. Moreover, the nuclear burning stages beyond He-burning are very short compared to those of hydrogen and helium. This is caused by the neutrino luminosity, which at $T_c \gtrsim 10^9$ K increases to such an extent that it become the main energy loss of the core. As $L_\nu \gg L$, the nuclear timescale is given by

$$\tau_{\text{nuc}} = \frac{E_{\text{nuc}}}{L_\nu} \quad (2.28)$$

Table 1. Stellar parameters and lifetime of each nuclear burning stage in a $15 M_{\odot}$ star (from Table I in Woosley et al. 2002)

Burning stage	T 10^9 [K]	ρ [g cm $^{-3}$]	L 10^3 [L_{\odot}]	R [R_{\odot}]	τ [yr]
Hydrogen	0.04	5.8	28.0	6.24	1.1×10^7
Helium	0.18	1.4×10^3	41.3	461	2.0×10^6
Carbon	0.83	2.4×10^5	83.3	803	2.0×10^3
Neon	1.63	7.2×10^6	86.5	821	0.7
Oxygen	1.94	6.7×10^6	86.6	821	2.6
Silicon	3.34	4.3×10^7	86.5	821	0.05

and leads to shortening lifetimes as shown in Table 1.

Super-asymptotic giant branch

In between the evolutionary paths of intermediate-mass and massive stars, there is a possible hybrid path. If the CO core has a mass slightly below the Chandrasekhar mass, the contraction leads only to a partial degeneracy of electrons. This allows the core to contract until it reaches $T_c \sim 10^9$ K, and turns on the neutrino cooling. As the outermost mildly-degenerate layers of the core lose energy via neutrinos, they contract further and reach higher temperatures. The subsequent ignition of a C-burning shell leads to a short-lived but highly luminous flash, which releases enough energy to develop convection in the shell and reduce the degeneracy in the layers below. Immediately after the first carbon flash ends, the contraction resumes and lead to another carbon flash, which now is able to expand subsonically inward and reach the core center. The second flash, also called flame due to its subsonic front, leaves behind a core enriched in neon, oxygen, and lighter elements. Following the second flash, a series of few other flashes take place at increasing height, while the oxygen-neon (ONe) core below grows in mass and contracts. When the carbon flashes stop, the stellar structure is constituted by a mildly-degenerate ONe core, a CO shell, a He-rich shell burning helium at its bottom, and an outer envelope (Nomoto 1984; Siess 2006; Doherty et al. 2017).

During the core contraction following the core He-burning, the envelope develops convection down to the bottom, as in the E-AGB phase. When the C-burning ends, the convective envelope bottom can extend till it gets close to the He-burning shell, and then initiate a series of thermal pulses as in the TP-AGB phase. Due to these similarities, this evolutionary phase is called super-asymptotic giant branch (SAGB), and it mainly differs from the AGB for the heavier cores and the shorter thermal pulsation period (Kip 2012, §34.8).

2.2. FORMATION OF THE COMPACT REMNANT

2.2.1 Core-collapse supernovae

Core collapse

The degenerate iron core grown in the late evolution of massive stars starts to contract as it exceeds the Chandrasekhar mass. The contraction is quickly turned into collapse at relativistic velocities by two processes. One is electron capture

$$p + e^- \rightarrow n + \nu_e , \quad (2.29)$$

which at $\rho \geq 10^7 \text{ g cm}^{-3}$ reach the equilibrium with its inverse reaction, the beta decay



and start to neutronize matter. This process consumes electrons, and decrease both degeneracy pressure and Chandrasekhar mass at the same time. Second one is iron photodisintegration, which sets in at $T_c \gtrsim 10^{10} \text{ K}$. At this temperature, the photons in the tail of Planck distribution have enough energy to break up iron nuclei into lighter elements. The photodisintegration drains a lot of energy from the radiation field, and thus decreases the radiation pressure. As the collapse increases temperature and density, the two processes become even more impactful and speed up the collapse.

The collapse is abruptly stopped when the matter reaches nuclear densities ($\rho \gtrsim 10^{14} \text{ g cm}^{-3}$), and nuclear forces together with neutron degeneracy pressure sustain the gravitational pull. This sudden halt of the collapse generates a bounce shock, that travels through the infalling matter and heats it. As the shock moves outward, the infalling matter gets heated to the point where nuclei disintegrate and a trail of neutrons and protons is left behind. In addition to the energy drained by nuclei disintegration, electron-capture ensue in the post-shock region, leading to a further energy loss by escaping neutrinos. About 10 ms after the collapse, the shock loses enough energy to stall.

The collapsed core, called proto-neutron star (PNS), accretes matter and contracts in the meanwhile. In doing so, the PNS pours a lot of neutrinos in the post-shock region, and quickly compensates for the losses by neutrino cooling. When neutrino heating ensues, it combines with several dynamical instabilities that can develop in the region below the shock, such as the Rayleigh-Taylor instability or the standing accretion shock instability (SASI). These instabilities convert the energy from the neutrino heating into kinetic energy between 0.1 and 1 s after the collapse, and when the kinetic energy overcome the ram pressure of the infalling matter the shock is revived. The time between the shock stall and its launch, which depends on the kind of instability involved, determines how much matter can be accreted onto the PNS.

The whole process is known as an iron core-collapse supernova (CCSN Woosley et al. 2002; Janka 2012), and it shred a massive star producing a compact object (namely a NS or a BH) and an ejecta. The mass ejected travels outward as a shock wave, triggering stellar formation, enriching the interstellar medium with heavy elements, and manifesting itself as a supernova remnant (SNR).

2.2.2 Electron-capture supernovae

While intermediate-mass stars generally end their life as white dwarfs, those undergoing SAGB can still end up in a supernova. In a SAGB star, after the carbon flashes cease, the partially-degenerate ONe core continues to contract. The contraction is initially led by neutrino cooling, but as temperature drops the neutrino production decreases. Since the core mass is still growing due to the shell burning above it, at a certain point the mass growth takes the place of neutrino cooling in leading the contraction. Mass growth not only makes the core contract, but raises T_c and ρ_c , and opens a bifurcation in the evolution of the star. If the mass of both CO shell and ONe core cannot grow above $1.37 M_\odot$, then the contraction lead to a complete-degeneration and the star eventually become a white dwarf. Instead, if the core as a whole manage to get above

Bounce and stall

Shock revival

Degenerate
carbon-burning

$1.37 M_{\odot}$ then the contraction leads to $\rho_c \gtrsim 10^{10} \text{ g cm}^{-3}$, triggering the electron capture by ^{24}Mg , ^{24}Na , and later ^{20}Ne . These reactions decrease the degeneracy pressure by electrons, and substitute the mass growth in leading the contraction.

Since the electron capture by ^{24}Mg , ^{24}Na , and ^{20}Ne , is exothermic, it also contributes to raise the core temperature. When the central temperature gets above $\sim 10^9 \text{ K}$, oxygen and neon are ignited at the center. The subsequent deflagration, however, does not release enough energy to either disrupt the core or to halt the contraction. Instead, electron capture from heavy nuclei and free electrons continues, and the collapse of the core accelerates. Since above the core there is only a light loose envelope, in contrast to the dense onion-like structure of massive stars, when the deflagration front reaches outward the envelope is easily ejected.

There is a broad consensus that this process, called electron-capture supernova (ECSN, Miyaji et al. 1980; Nomoto 1987; Siess 2007; Takahashi et al. 2013), ends with an electron-capture driven collapse and the formation of a NS together with a rather symmetric ejecta (Poelarends et al. 2008; Doherty et al. 2015). Nevertheless, recent simulations have shown that the oxygen deflagration can possibly overcome the contraction and disrupt the core, leaving no remnant (Jones et al. 2016).

2.3. BIRTH PROPERTIES OF NEUTRON STARS

2.3.1 Mass

After the PNS settles down, the stellar core either became a NS or a BH. In both cases the result is a compact object, since the NS have a radius that is only few times that of a BH with the same mass. Therefore, to get a basic understanding of the structure of a NS we have to take into account general relativity.

Let us assume as a first-order approximation that NSs are spherically-symmetric non-rotating bodies. By the Birkhoff's theorem, we know that the spacetime metric around such an object is given by the Schwarzschild solution to Einstein's vacuum field equations, $G_{\mu\nu} = 0$. The metric inside the object, on the other hand, can be obtained solving the Einstein field equations

$$G_{\mu\nu} = \frac{8\pi G}{c^4} T_{\mu\nu}, \quad (2.31)$$

and matching the interior metric with the exterior metric at the body surface. Working again with a first-order approximation, we can do this assuming that the body is a perfect fluid with isotropic pressure and hydrostatic equilibrium, so that

$$T^{\mu\nu} = \left(P + \frac{\rho}{c^2} \right) u^\mu u^\nu + Pg^{\mu\nu} \quad (2.32)$$

where P is the pressure, ρ is the rest-frame mass density, and u^μ is the four-velocity field. The resulting exterior metric have a degree of freedom which can be fixed by expliciting the equation of state, namely $P = P(\rho)$ (for the full derivation see Wald 1984 §6.2). Having fixed the geometry of spacetime and hence the mass distribution, we can exploit the local conservation of the

Electron capture and
ONe deflagration

Tolman-Oppenheimer-
-Volkoff equation



Figure 6. The Crab Pulsar (bright spot at center), the NS residing in the center of the Crab Nebula. Due to the fast rotation of the NS and its powerful magnetic field, the surrounding matter is funneled into an axisymmetrical wind-powered nebula, whose structure clearly shows a torus and two jets. The Crab Nebula (not fully shown) is widely recognized as the SNR left from the birth of the Crab Pulsar. This composite image is made of observations from *Spitzer* (infrared, in purple), *Hubble* (optical, in blue), and *Chandra* (X-ray, in white) *Space Telescopes*. Credit: X-ray: NASA/CXC/SAO; Optical: NASA/STScI; Infrared: NASA-JPL-Caltech

stress-energy tensor, $T^{\mu\nu}_{;\nu} = 0$, to obtain the equation of motion of the gas

$$\frac{dP}{dr} = -\frac{Gm\rho}{r^2} \left(1 + \frac{P}{\rho c^2}\right) \left(1 + \frac{4\pi r^3 P}{mc^2}\right) \left(1 - 2\frac{Gm}{rc^2}\right)^{-1} \quad (2.33)$$

called the Tolman-Oppenheimer-Volkoff (TOV) equation (Tolman 1939; Oppenheimer and Volkoff 1939). This equation is the general-relativistic analog of (2.2), constraining the structure of the NS from the condition of hydrostatic equilibrium.

Neutrons, being fermions, are able to become degenerate, and the conditions in NSs are such that their neutrons are highly degenerate. Similarly to degenerate cores, the degeneracy pressure is what prevents in the first place the collapse of a NS and sustains its hydrostatic equilibrium, but only if the mass is below a critical value. The seminal work from Oppenheimer and Volkoff (1939) placed the maximum value for NS mass to $0.7 M_{\odot}$. However, this result was obtained assuming that neutrons do not interact, while in fact neutron-neutron interactions are quite relevant since the physical conditions involved. When accounting for the repulsion from strong interaction, and the removal of electron by production of new particle such as pions or hyperons, the maximum mass increases. Recent estimations gives values as high as $3 M_{\odot}$, which are in agreement with the observed distribution from Galactic BNSs which is centered at $1.33 M_{\odot}$ and has a dispersion of $0.09 M_{\odot}$ (Özel and Freire 2016).

Mass range

Momentum-conserving
natal kick

The hydrodynamical instabilities that arise during SN explosions can cause relevant asymmetries in the distribution of matter ejected. This implies that the ejecta as a whole can carry away a relevant amount of linear momentum p_{ej} , and if we assume that linear momentum is conserved during the explosion then the compact remnants should get recoiled. That is to say, if after the explosion holds

$$p_{\text{ns}} = p_{\text{ej}} \quad (2.34)$$

where $p_{\text{ns}} = v_{\text{ns}} M_{\text{ns}}$ is the linear momentum of the NS, then the NS must acquire a natal velocity equal to

$$v_{\text{ns}} = \frac{p_{\text{ej}}}{M_{\text{ns}}} , \quad (2.35)$$

commonly known as natal kick.

As shown by Scheck et al. (2006), a deeper understanding of this process can be obtained through the Euler equation

$$\rho \frac{\partial \mathbf{v}}{\partial t} + \rho(\mathbf{v} \cdot \nabla) \mathbf{v} = -\nabla P - \rho \nabla \Phi , \quad (2.36)$$

where Φ is the Newtonian gravitational potential. Integrating (2.36) over a control surface Σ that encloses the PNS, we get its integral form

$$\dot{\mathbf{p}}_{\text{ns}} = - \int_{\Sigma} P \hat{\mathbf{n}} d\sigma - \int_{\Sigma} \rho(\mathbf{v} \cdot \hat{\mathbf{n}}) \mathbf{v} d\sigma + \int_{M_{\text{ej}}} G M_{\text{ns}} \frac{\mathbf{r}}{r^3} dm \quad (2.37)$$

which shows the different contributions to the kick, and if integrated over time gives another estimate of v_{ns} . On the right hand side of (2.37), the first term accounts for external pressure, the second accounts for the mass accreted or ejected, and the third for the gravitational attraction of the surrounding matter. The third term gives rise to the so-called gravitational tug-boat mechanism. Equation (2.37) is an approximation since we are neglecting the viscous terms, but several simulations have shown that it is a good approximation and indeed linear momentum is conserved to a good degree (Wongwathanarat et al. 2013).

Observational velocity
distribution

From the observational point of view, the distribution of natal kick magnitudes is still a matter of debate. Historically, a well receive results is that the population of Galactic pulsars shows a velocity distribution with one single peak at high values (Lyne and Lorimer 1994), and the latest results showed that the natal kick distribution can be fitted by a Maxwell distribution with $\sigma = 265 \text{ km s}^{-1}$ (Hobbs et al. 2005). Furthermore, also certain Galactic BNSs seems to need strong kicks to be explained (Fryer and Kalogera 1997). However, the picture where NSs receive only high kicks are in tension with results from both Galactic pulsars (Arzoumanian et al. 2002; Verbunt et al. 2017) and Galactic BNSs (Beniamini and Piran 2016). These results points toward a bimodal distribution of velocities, with a peak at small values that can even dominate the distribution. The scenario in which natal kicks can have both high and low magnitudes can also account for other observations, such as those from the X-ray binaries⁶ (Pfahl et al. 2002; Knigge et al. 2011), and is highly compatible with SN mechanisms that produce low-mass ejecta like the ECSNe (van den Heuvel 2007).

⁶X-ray binaries are binary systems composed of a star and a compact object (either a BH or a NS), in which there the compact object is accreting mass from the star. The binary manifests as an X-ray source due to various physical processes taking place during the accretion

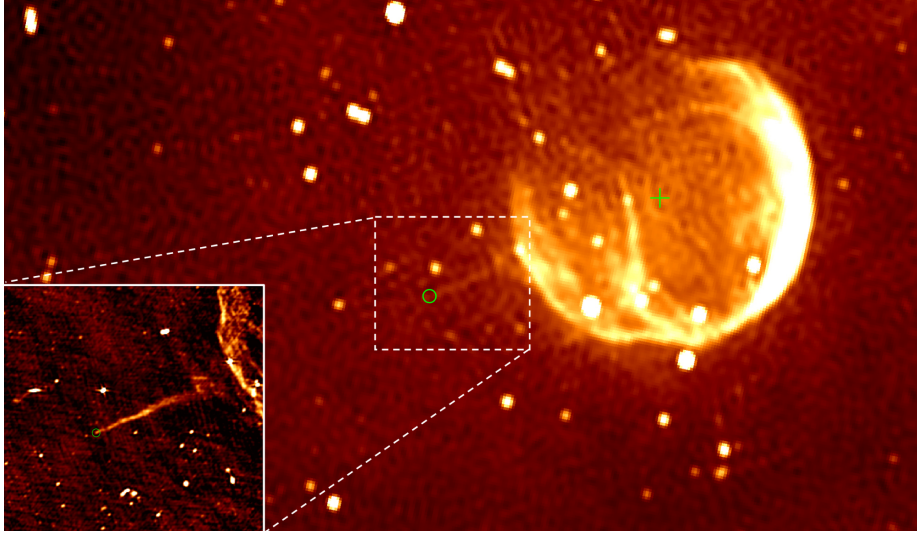


Figure 7. The pulsar PSR J0002+6216, also known as the Cannonball Pulsar. The NS is traveling away from the supernova remnant CTB 1 at more than 1000 km s^{-1} , leaving behind a glowing trail of shocked material. The NS was likely born in the same SN that produced CTB 1. The position of the NS is marked with a green circle, while the geometrical center of the SNR is marked with a green cross. Figure from Schinzel et al. (2019).

2.3.3 Spin and magnetic field

Assuming that both NS and progenitor star are a spherical body with a moment of inertia equal to

$$I = \frac{2}{5}MR^2, \quad (2.38)$$

if we roughly assume that during the SN the angular momentum is conserved

$$I\Omega = I_{\text{ns}}\Omega_{\text{ns}}, \quad (2.39)$$

then we have

$$\Omega_{\text{ns}} = \Omega \frac{MR^2}{M_{\text{ns}}R_{\text{ns}}^2} \Rightarrow \mathcal{P}_{\text{ns}} = \mathcal{P} \frac{MR^2}{M_{\text{ns}}R_{\text{ns}}^2} \quad (2.40)$$

where \mathcal{P} is the period. Assuming typical values, such as

$$\mathcal{P} \sim 10^5 \text{ s}, \quad M \sim 10 \text{ M}_\odot, \quad R \sim 6 \text{ R}_\odot,$$

$$M_{\text{ns}} \sim 1 \text{ M}_\odot, \quad R_{\text{ns}} \sim 2 \times 10^{-5} \text{ R}_\odot,$$

we obtain

$$\mathcal{P}_{\text{ns}} \approx 10^{-3} \text{ s}, \quad (2.41)$$

which is in agreement with the observed period of pulsars, ranging from 10^{-3} to 10 s. It is worth noting that $\mathcal{P} = 10^{-3}$ s is equivalent to 1000 rotations per second.

In a similar way, if we assume that the magnetic flux is conserved during the collapse

$$BR^2 = B_{\text{ns}}R_{\text{ns}}^2, \quad (2.42)$$

Magnetic dipole model

where B is the magnetic field at the surface, using $B \sim 100$ G as typical value we get

$$B_{\text{ns}} \approx 10^{12} \text{ G} , \quad (2.43)$$

which is again coherent with the observations, and even not the strongest value measured.

The coupling between rotation and the magnetic field is one of the main effects governing the evolution of a NS. If we assume that the strong magnetic field is in first-order approximation a dipole, then a misalignment between the magnetic and rotational axes leads to the emission of electromagnetic radiation. Assuming a misalignment angle α , the energy carried away by the dipole emission can be estimated with the Larmor formula

$$\dot{E}_{\text{dip}} = -\frac{1}{6c^3} B^2 R^6 \Omega^4 \sin^2 \alpha , \quad (2.44)$$

and if we consider that the main energy reservoir involved in the motion is the rotational kinetic energy

$$E_{\text{rot}} = \frac{1}{2} I \Omega^2 \quad (2.45)$$

which has time derivative $\dot{E}_{\text{rot}} = I \Omega \dot{\Omega}$, then from the energy balance we have

$$\dot{\Omega} = -\frac{B^2 R^6 \Omega^3 \sin^2 \alpha}{6Ic^3} . \quad (2.46)$$

Since the right hand side is negative, equation (2.46) shows the how the NS spin slows down due to magneto-rotational braking.

From (2.46) we can get the classic vacuum magnetic dipole estimate for the surface magnetic field

$$B \approx 3.2 \times 10^9 \sqrt{P \dot{P}} \text{ G} . \quad (2.47)$$

Also, from the integration in time of (2.46) we can estimate the timescale on which the spin slows down to a certain value

$$\tau_c = -\frac{1}{2} \frac{\Omega}{\dot{\Omega}} = \frac{1}{2} \frac{P}{\dot{P}} , \quad (2.48)$$

which can be used to estimate the NS age and is called characteristic age (Shapiro and Teukolsky 1983, §10.5). This last estimate is reliable if the initial spin velocity is much higher than the observed velocity, and the NS has not been spun-up (for example, by mass accretion).

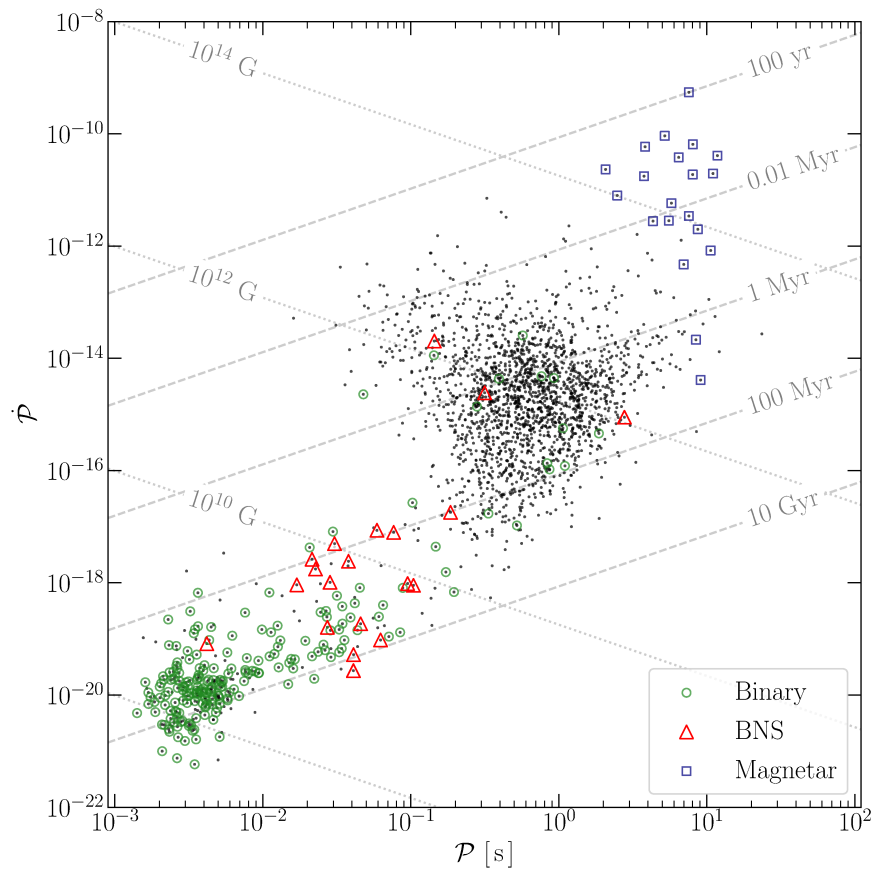


Figure 8. \mathcal{P} - $\dot{\mathcal{P}}$ diagram of the NSs in the ATNF Pulsar Catalogue (Manchester et al. 2005). Plain dots are observed Galactic pulsars, while magnetars and pulsars bounded in binary systems are properly marked. The grey lines show level curves of both the surface magnetic field and the characteristic age, given respectively by (2.47) and (2.48). The catalogue can be found online at <http://www.atnf.csiro.au/research/pulsar/psrcat>.

CHAPTER 3

Binary neutron stars

This Chapter presents the current models of the main evolutionary processes in isolated binary stars. These binary processes are then integrated with the single stellar evolution framework to outline two main scenarios for the formation of BNSs.

Part of this Chapter is based on the lecture notes of Pols (2011) on binary stars.

3.1. STELLAR EVOLUTION OF BINARY STARS

3.1.1 Grounding ansatz

As far as we know, BNS can form as a result of the stellar dynamics in crowded environment such as star clusters, but this dynamical formation channel seems not so efficient (Sadowski et al. 2008; Belczynski et al. 2018). Instead, we know that almost every massive star belongs to a binary system, and we know that they can evolve into NSs (Sana et al. 2012). Following these two premises another formation channel emerges, namely the evolutionary channel, in which binary stars evolve directly into BNSs through stellar evolution alone. This formation channel is open to all those binaries that do not experience dynamical interactions, such as all the field binaries (Tauris et al. 2017).

The formation of a BNS cannot be modeled within the bare framework established in Chapter 2, and the reason is simple: stars interact when they are together. Currently, we know ~ 20 Galactic BNSs among the ~ 3000 NSs observed in our Galaxy (Manchester et al. 2005). Most of them are isolated field binaries, hence they have been likely formed through the evolutionary channel. By looking at their properties we see a trend in the semi-major axis: most orbits are closer than few solar radii (Table 2). Also the observed BNS mergers point in this direction, since they could not have been merged within a Hubble time if they were formed with orbits wider than $\sim 4.5 R_{\odot}$ ¹. So, a simple question arises: if they are born as binary stars, and stars during their evolution swell up to $10^3 R_{\odot}$, how do they get so close?

The answer must lie in the fact that the evolution of binary stars is more than the evolution of two single stars. We know through observations that there is plenty of processes shaping both the stellar and orbital evolution of binary stars, such as mass exchanges, common envelopes, kicks, and so on. These binary processes provide a framework for the modelization of the evolutionary channel, which must emerge as a certain combination of these interactions, and should permit a binary star to survive up to two SNe until it becomes a BNS.

3.1.2 Mass transfer

To understand how mass can be exchanged between two stars, we need first to understand the gravitational potential in a binary system. Let us restrict

Roche potential

¹Assuming a circular orbit and both NSs weighting $1.36 M_{\odot}$.

Table 2. Parameters of Galactic BNSs

Pulsar	\mathcal{P}_{orb} [days]	e	a [R _⊕]	M_{puls} [M _⊕]	M_{comp} [M _⊕]	Ref.
J0453+1559	4.072	0.113	15.998	1.559	1.174	a
J0737-3039	0.102	0.088	1.261	1.338	1.249	b
B1534+12	0.421	0.274	3.284	1.333	1.346	c
J1756-2251	0.320	0.181	2.696	1.341	1.230	d
B1913+16	0.323	0.617	2.801	1.440	1.389	e
J1913+1102	0.206	0.090	2.088	1.580	1.300	f
J1757-1854	0.184	0.606	1.903	1.338	1.395	g
J1906+0746 †	0.166	0.085	1.750	1.291	1.322	h
J1807-2500B ‡‡	9.957	0.747	26.690	1.366	1.206	i
B2124+11C ‡	0.335	0.681	2.829	1.358	1.354	j
J1755-2550 †*	9.696	0.089	26.701	-	-	k
J1518+4904 *	8.634	0.249	24.714	-	-	l
J1811-1736 *	18.779	0.828	41.487	-	-	m
J1829+2456 *	1.176	0.139	6.542	-	-	n
J1930-1852 *	45.060	0.399	74.357	-	-	o
J1753-2240 *	13.638	0.304	33.519	-	-	p
J1411+2551 *	2.616	0.169	11.149	-	-	q
J1946+2052 *	0.078	0.064	1.072	-	-	r

Notes. † Not confirmed. ‡ Belongs to a globular cluster. * Semi-major axis is computed assuming both components weight 1.36 M_⊕ each.

References. (a) Martinez et al. (2015). (b) Kramer et al. (2006). (c) Fonseca et al. (2014). (d) Faulkner et al. (2005). (e) Hulse and Taylor (1975). (f) Lazarus et al. (2016). (g) Cameron et al. (2018). (h) van Leeuwen et al. (2015). (i) Lynch et al. (2012). (j) Jacoby et al. (2006). (k) Ng et al. (2018). (l) Janssen et al. (2008). (m) Corongiu et al. (2007). (n) Champion et al. (2004). (o) Swiggum et al. (2015). (p) Keith et al. (2009). (q) Martinez et al. (2017). (r) Stovall et al. (2018).

to circular orbits for the sake of conciseness². To study of the dynamics inside a binary, a smart frame of reference is the one located at the barycenter and co-rotating with the stars, so that the bodies seem stationary. In such frame of reference, if we assume that stars behave like point masses³, then the motion of a mass particle can be formulated as a restricted 3-body problem. From this point of view, the mass particle moves in the Roche potential

$$\Psi = -\frac{\mathcal{G}M_1}{\|\mathbf{r} - \mathbf{r}_1\|} - \frac{\mathcal{G}M_2}{\|\mathbf{r} - \mathbf{r}_2\|} - \frac{1}{2}(\boldsymbol{\omega} \times \mathbf{r})^2 \quad (3.1)$$

which includes the gravitational pull of the two stars and the centrifugal force. Here \mathbf{r} is the position of the particle, \mathbf{r}_1 and \mathbf{r}_2 are the positions of the two stars, and $\boldsymbol{\omega}$ is the angular velocity vector.

Let us assume that stars are made of an ideal fluid in hydrostatic equilibrium. An isolated star must satisfy (2.2), which can be recast in vectorial form as

$$\nabla P = \rho \nabla \Phi \quad (3.2)$$

²Close binaries are quickly circularized by tides.

³This is a reasonable approximation as long as the stellar structure is composed by a heavy dense core, and a light lose envelope.

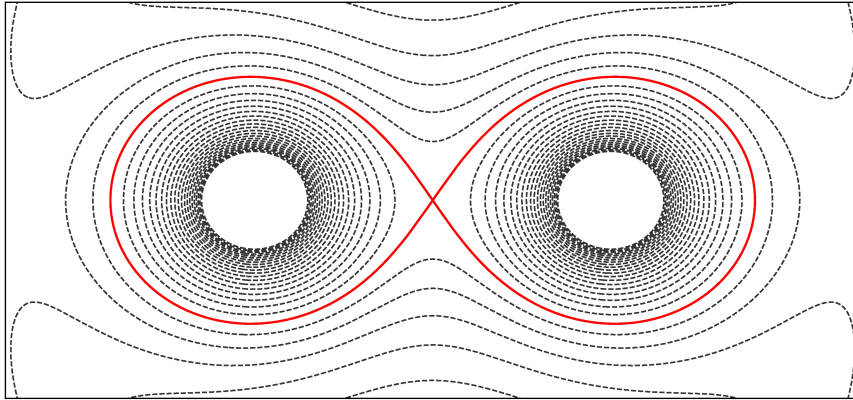


Figure 9. Contour plot of the Roche potential for two equal masses. The red contour line locates the two Roche lobes, which met at the first Lagrangian point.

with Φ being the Newtonian gravitational potential, whereas the components of a binary star are constrained by

$$\nabla P = \rho \nabla \Psi \quad (3.3)$$

where Ψ is the Roche potential. In a static condition the bodies to fill an equipotential surface, so in the Roche potential the binary can either be in one of three configurations, depending on how many components touch the inner equilibrium point, called the first Lagrangian point. In the first configuration, none of the two components reach the Lagrangian point, and the system is called detached. In the second configuration, one component reaches the Lagrangian point, and the system is called semi-detached. This is a critical configuration because the equilibrium point belongs to two equipotential surfaces, each one enclosing a different star. Hence, a particle moving on these surfaces can cross the Lagrangian point and shift from the gravitational influence of one star to the other. The two drop-like surfaces are called Roche lobes, and they are grounds for mass transfer since all the mass that goes beyond them can be transferred to the companion. A third configuration exists, in which both stars reach the Lagrangian point and fill their Roche lobe, and the system is called a contact binary (Pols 2011, §6.1).

Roche lobe overflow

A handy approximation for the Roche lobe size is given its effective radius, which is the radius of a sphere with the same volume of the lobe. An easy formula is given by Eggleton (1983)

$$R_L = \frac{0.49 q^{2/3}}{0.6 q^{2/3} + \ln(1 + q^{1/3})} a \quad (3.4)$$

where q is the mass ratio, and a is the semi-major axis.

Since stars expand during certain evolutionary phases, they can eventually end up filling their Roche lobe. When this happens, the matter that crosses the lobe goes through the first Lagrangian point and falls into the companion's lobe. At this stage the two stars are usually identified as donor and accretor.

Whenever the accretor is much smaller than its Roche lobe, the transferred mass is collected on an accretion disk and from there it starts to spiral-in toward the star. The mass transfer can also be triggered by a decrease of the semi-major axis, which shrinks also the Roche lobe. This mass transfer process is known as Roche lobe overflow (RLO, [Pols 2011](#), §7).

Stability of RLO

The stability of the RLO is dictated by the reaction of the donor to the mass loss. If after a small mass transfer the stellar radius get smaller than R_L , then the transfer is halted until the Roche lobe is crossed again, and the RLO is said stable. Otherwise, when after a small transfer the stellar radius is still bigger than the R_L , the mass transfer continues and the RLO is said unstable. The case of unstable RLO is complicated by the fact that mass loss can remove the star from both its conditions of hydrostatical and thermal equilibrium, hence it can trigger reactions on both a dynamical timescale τ_{hydro} and a thermal timescale τ_{KH} .

Following [Webbink \(1985\)](#), let us evaluate the stability by means of three parameters: the Roche mass-radius exponent

$$\zeta_L = \frac{d \log R_L}{d \log M}, \quad (3.5)$$

the adiabatic mass-radius exponent

$$\zeta_{\text{ad}} = \left(\frac{d \log R}{d \log M} \right)_{\text{ad}}, \quad (3.6)$$

and the equilibrium mass-radius exponent

$$\zeta_{\text{eq}} = \left(\frac{d \log R}{d \log M} \right)_{\text{eq}}. \quad (3.7)$$

Upon mass transfer, the star react either contracting or expanding. The reaction first aim to reestablish the hydrostatic equilibrium, which happens on a dynamical timescale τ_{hydro} through an adiabatic transformation characterized by ζ_{ad} . Then, the reaction proceeds to reestablish the thermal equilibrium on a thermal timescale τ_{KH} , through a variation characterized by ζ_{eq} .

The stable and unstable cases of RLO emerge from the comparison between these two exponent and ζ_L , which accounts for the variation of R_L following a change in the mass ratio. We can distinguish three different cases: the stable, the thermally unstable, and dynamically unstable RLO (see [Figure 10](#)). The stable case is characterized by $\zeta_L < \min\{\zeta_{\text{ad}}, \zeta_{\text{eq}}\}$, which means that as the donor loses mass, the effective radius of the Roche lobe decreases slower than the radius needed for total equilibrium (it can even increase). When $\zeta_{\text{eq}} < \zeta_L < \zeta_{\text{ad}}$ the RLO is said thermally unstable. In this case, the Roche lobe decrease more rapidly than the radius needed for thermal equilibrium and hence the mass transfer proceeds. The mass transfer rate slowly varies on a thermal timescale, and the process is self-regulating (hence is stable in practice). When $\zeta_{\text{ad}} < \zeta_L$, the RLO is said dynamically unstable. As the star loses mass, R_L decreases so fast that even the hydrostatical equilibrium is perturbed. This transfer triggers a reaction on a dynamical timescale, which eventually leads to a runaway process and the subsequent spiral-in of the two stars.

A second way to classify RLO is through the donor's evolutionary phase.

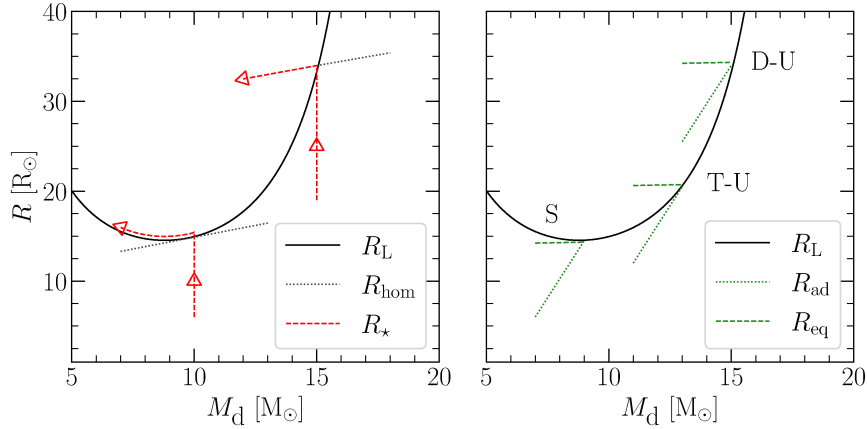


Figure 10. Left: Schematic evolution of the mass transfer in two binaries with a total mass of $20 M_{\odot}$ and an orbital separation of $150 R_{\odot}$. It is assumed that the stellar radius scales with the homology relation $R \propto M^{0.8}$. In the case of a $10 M_{\odot}$ donor, when the star fills the Roche lobe and triggers the RLO, the mass loss widens the orbit together with the Roche lobe. Thus, the donor must expand again before losing other mass, and hence the stellar radius evolves following the Roche lobe. In the case of a $15 M_{\odot}$ donor, the mass transfer causes the Roche lobe to shrink more rapidly than the size of the star, leading to an unstable mass transfer. Right: Representation of the conditions for stable (S), thermally-unstable (T-U), and dynamically-unstable (D-S) RLO (see the text for an explanation). The exponents have arbitrarily chosen to be $\zeta_{\text{eq}} = 0.25$ and $\zeta_{\text{ad}} = 1.5$. Figures adapted from [Pols \(2011\)](#).

The RLO started in the donor's MS is said case A, the one started during shell H-burning is said case B, and the one occurring during shell He-burning is said case C. Moreover, RLO can occur also in stars that have lost their envelope, either because of mass loss or mass transfer. In this case, we refer to the RLO as case BA if the donor is in core He-burning, case BB during shell He-burning, and case BC during C-burning (see Figures 3 and 4). The link between this classification and the previous is given by the thermal structure of the stars: as explained clearly by [Webbink \(1985\)](#), stable RLOs are produced by radiative envelopes, while unstable RLOs are produced by convective envelopes.

There is another mass transfer mechanism in addition to RLO, which is wind accretion. In binary stars, the mass lost by one star through winds can be deflected by the gravitational attraction of the companion, and thus accreted. A simple but useful model is given by the Bondi-Hoyle spherical accretion, which differs from wind accretion by the fact that it is spherically symmetric, and hence must be parameterized to account for a partial accretion (e.g. [Hurley et al. 2002](#)).

Both RLO and wind accretion induce a variation in the orbit of the binary. Indeed, mass transfer changes not only the mass of the single components, but also the angular momentum of the binary. Assuming that the spin angular momentum of the stars is negligible with respect to the orbital angular momentum, and a circular orbit, the total angular momentum of the binary is

$$J = M_d M_a \sqrt{\frac{G a}{M_d + M_a}} \quad (3.8)$$

Orbital evolution

where M_d and M_a are respectively the masses of donor and accretor, and its time derivative is then

$$\frac{\dot{J}}{J} = \frac{1}{2} \frac{\dot{a}}{a} + \frac{\dot{M}_d}{M_d} + \frac{\dot{M}_a}{M_a} - \frac{1}{2} \frac{\dot{M}_d + \dot{M}_a}{M_d + M_a} \quad (3.9)$$

In the case of a conservative transfer, that is to say

$$\dot{M}_a = -\dot{M}_d \quad \text{and} \quad \dot{J} = 0 ,$$

equation (3.9) gives

$$\frac{\dot{a}}{a} = 2 \left(\frac{M_d}{M_a} - 1 \right) \frac{\dot{M}_d}{M_d} . \quad (3.10)$$

Since $\dot{M}_d < 0$ by definition, (3.10) shows that \dot{a} is positive only if $M_d < M_a$, and hence that a mass transfer with $M_d > M_a$ lead to a shrinking orbit (Verbunt 1993).

In the case of a non-conservative transfer, that is to say

$$\dot{M}_a = -\beta \dot{M}_d \quad \text{and} \quad \dot{J} \neq 0$$

where β is the ratio of mass accreted to mass lost from the donor, the binary loses both mass and angular momentum. We can quantify \dot{J} assuming that the specific angular momentum lost is a fraction α of the specific angular momentum of the binary

$$\frac{\dot{J}}{\dot{M}_d + \dot{M}_a} = \alpha \frac{J}{M_d + M_a} , \quad (3.11)$$

so we can substitute it into (3.9) to get

$$\frac{\dot{a}}{a} = -\frac{\dot{M}_d}{M_d} \left[2 - 2\beta \frac{M_d}{M_a} - (1 - \beta)(1 + 2\alpha) \frac{M_d}{M_d + M_a} \right] . \quad (3.12)$$

However, even with an operative expression for \dot{a} we cannot draw many conclusions, since both α and β deeply depends on the physics assumed for both star and mass transfer (Verbunt 1993).

Please notice that this brief exposition is just a primer on mass transfer in binary stars, since we have neglected the role of eccentricity, the effects on the stars' spin, and stellar processes such as the the accretor rejuvenation.

3.1.3 Common envelope

CE formation

Alongside the mass transfer, there is another process that has a major role in shaping the evolution of a binary star: the common envelope (CE) process (Paczynski 1976; Webbink 1984). During a CE phase, the binary is in a configuration similar to a contact binary, but with the cores orbiting each other while embedded in a decoupled common envelope (hence the name).

A binary star can get to a CE through different paths. The first one is a dynamically unstable RLO, in which the donor expands way over the Roche lobe until its envelope reaches and engulfs the other star. The second one is a RLO in which the accretor is not able to adjust its structure to the accreted matter, and eventually end up filling its Roche lobe. A third path is through orbital instabilities, such as the Darwin instability or resonances, which can both lead to a spiral-in or a collision of the stars.

The physics underlying the process is still poorly understood, but hydrodynamical simulations have built consensus on four main phases of the CE evolution. Following Ivanova et al. (2013), the first phase is the formation of a common envelope and the loss of corotation, which can take place on a timescale between the dynamical and the thermal. The second phase is a fast spiral-in of the cores on a dynamical timescale. During this plunge-in, the cores deposit energy in the envelope through dissipative phenomena, and the envelope eventually starts to expand. The third phase is a slow spiral-in taking place on a thermal timescale, following by the fourth phase which is its termination. At the end of the process, the two cores are either merged during the fast spiral-in or have successfully ejected the envelope and formed a close binary.

Since the complexity posed by the process, a realistic analytical model is hard to obtain. Reasonable predictions are obtained from a properly parametrized energy balance, also known as $\alpha\lambda$ -formalism (e.g. Hurley et al. 2002). In this formalism, the gravitational binding energy of the envelopes prior to the ejection is

$$E_{\text{bin,in}} = -\frac{\mathcal{G}M_1 M_{1,\text{env}}}{\lambda_1 R_1} - \frac{\mathcal{G}M_2 M_{2,\text{env}}}{\lambda_2 R_2} \quad (3.13)$$

where λ is a free parameter which accounts for the stellar structure and may include the internal energy, M_{env} is the envelope mass, and R is the stellar radius before the CE. Considering the orbital energy of the cores at the onset of CE

$$E_{\text{orb,in}} = -\frac{\mathcal{G}M_{1,\text{core}} M_{2,\text{core}}}{a_{\text{in}}} \quad (3.14)$$

and after it

$$E_{\text{orb,fin}} = -\frac{\mathcal{G}M_{1,\text{core}} M_{2,\text{core}}}{a_{\text{fin}}} , \quad (3.15)$$

we can assume the difference between the two to be caused by energy deposition into the envelope by dissipative mechanisms. Hence, if we assume that after the CE event the whole envelope gets ejected, that is $E_{\text{bin,fin}} = 0$, the energy balance reads

$$\Delta E_{\text{bin}} = -\alpha_{\text{CE}} \Delta E_{\text{orb}} \quad (3.16)$$

where α_{CE} is free parameter which accounts for the efficiency of the energy deposition. This formulation can be corrected to account for the retention of an envelope fraction. From (3.16) we can have a prediction of the binary's fate, whether it ends up in a merger or shranked down to a_{fin} . Recent findings have shown that the parameters α_{CE} and λ are highly dependent on the stellar structure and the physics behind the ejection, so they have turned out to be quite a complication even if they were introduced as simplifications (Ivanova et al. 2013).

3.1.4 Kicks

We have shown in Section 2.3.2 that the mass ejection during the SN explosion can cause the NS to recoil, imparting the so-called natal kick. When a binary star is considered, the effect of this instantaneous mass loss is twofold: it gives a kick to the NS, but also removes mass and angular momentum from the binary. We can idealize this process as the sum of two separate mass ejections, one spherically symmetric and the other asymmetric. The first one imparts what

CE evolution

Energy balance

is known as the Blaauw kick (Blaauw 1961; Boersma 1961), while the second imparts the natal kick (see §2.3.2).

Blaauw kick

Starting from the symmetric ejection, let us notice that if we approximate the SN to be instantaneous, then the positions of the stars are preserved. Since the orbit gets widened by the mass ejection, the position prior the SN must become the periastron of the orbit after the SN, that is to say

$$a_{\text{in}} = a_{\text{fin}}(1 - e) \quad (3.17)$$

where a_{in} is the stars' distance prior the SN, a_{fin} and e are the semi-major axis and the eccentricity after the SN. Under the assumption that also the orbital velocity is conserved during the SN, given the velocity before

$$v_{\text{in}}^2 = \frac{\mathcal{G}M_{\text{tot}}}{a_{\text{in}}} \quad (3.18)$$

and after the mass ejection

$$v_{\text{fin}}^2 = \mathcal{G}(M_{\text{tot}} - M_{\text{ej}}) \left(\frac{2}{a_{\text{in}}} - \frac{1}{a_{\text{fin}}} \right) \quad (3.19)$$

where $M_{\text{tot}} = M_1 + M_2$ is the total mass prior the SN, and M_{ej} is the ejected mass, we can equate them to obtain

$$e = \frac{M_{\text{ej}}}{M_{\text{tot}} - M_{\text{ej}}} . \quad (3.20)$$

This last equation gives us the final eccentricity, the final semi-major axis upon substituting it in (3.17), and under the constrain $e < 1$ it shows that for $M_{\text{ej}} \geq M_{\text{tot}}/3$ the binary unbinds (Verbunt 1993).

Natal kick

Regarding the asymmetric ejection, we have notice that it gives the star an impulse likely due to linear momentum conservation. Calling \mathbf{v}_{in} the velocity just before the SN, then the velocity just after the SN is

$$\mathbf{v}_{\text{fin}} = \mathbf{v}_{\text{in}} + \mathbf{v}_k \quad (3.21)$$

where \mathbf{v}_k is the kick velocity. If we substitute the norm of \mathbf{v}_{fin}

$$v_{\text{fin}}^2 = v_{\text{in}}^2 + v_k^2 + 2 |\mathbf{v}_{\text{in}} \cdot \mathbf{v}_k| , \quad (3.22)$$

into (3.19), we can obtain the semi-major axis after the SN

$$a_{\text{fin}} = \frac{\mathcal{G}a_{\text{in}}}{2\mathcal{G}M_{\text{tot}} - v_{\text{fin}}^2 a_{\text{in}}} \quad (3.23)$$

where we have assumed $M_{\text{ej}} = 0$ for semplicity. The new eccentricity can be obtained from the specific angular momentum

$$\mathbf{h}_{\text{fin}} = \mathbf{a}_{\text{fin}} \times \mathbf{v}_{\text{fin}} , \quad (3.24)$$

since for its norm holds the relation

$$h_{\text{fin}}^2 = \mathcal{G}M_{\text{tot}}a_{\text{fin}}(1 - e^2) \quad (3.25)$$

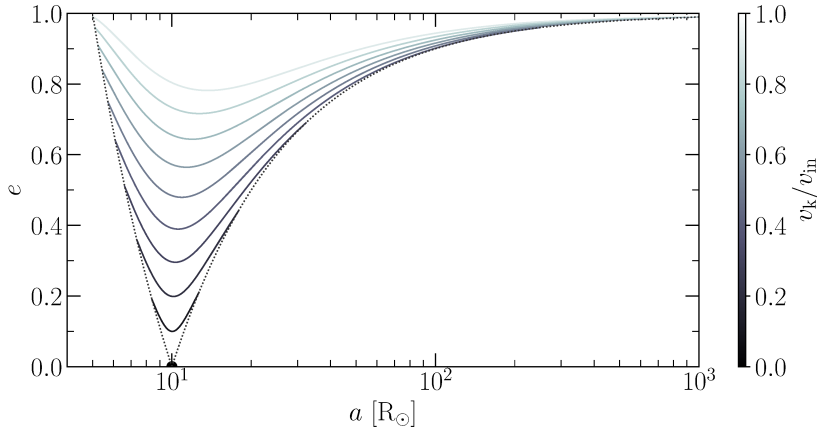


Figure 11. Effect of a natal kick on the orbit of a binary system. The primary weights $1 M_{\odot}$, the secondary weights $10 M_{\odot}$, and the orbit has $e = 0$ and $a = 10 R_{\odot}$. The natal kick vector is assumed to be lying in the orbital plane. Each continuous line has obtained imparting a natal kick with fixed norm (encoded by the color as a fraction of the initial orbital velocity) and varying its orientation with respect to the orbital velocity. The two dotted lines show the geometrical limits beyond which either the orbit becomes open, or there are no possible configurations.

which gives

$$e^2 = 1 - \frac{h_{\text{fin}}^2}{GM_{\text{tot}}a_{\text{fin}}} . \quad (3.26)$$

Figure 11 shows the change in eccentricity and semi-major axis of a circular orbit due to a natal kick, as function of the kick's norm. Note that since \mathbf{v}_{in} is not parallel to \mathbf{v}_{fin} , also \mathbf{h}_{in} is not parallel to \mathbf{h}_{fin} , and hence another effect of natal kick is the tilting of the orbital plane.

A unified formulation for both kicks, taking into account also a non-zero initial eccentricity, can be found in Hurley et al. (2002).

3.1.5 Gravitational waves

In the context of the general theory of relativity, gravitational waves are solutions of the Einstein field equations that propagate as waves and show a bosonic behavior. They are usually presented in the non-relativistic weak-field regime, where they appear as perturbations of the metric that travel as plane waves across a Minkowskian spacetime.

In the weak-field limit, GWs show striking similarities with the electromagnetic waves. Let us follow Zee (2013). In electromagnetism, the field equations are the Maxwell equations in vacuum

$$\partial_{\mu}F^{\mu\nu} = 0 \quad (3.27)$$

where $F_{\mu\nu} = \partial_{\mu}A_{\nu} - \partial_{\nu}A_{\mu}$ is the electromagnetic field tensor, and A_{μ} is the electromagnetic four-potential. Imposing the Lorenz gauge $\partial_{\mu}A^{\mu} = 0$ and fixing the residual gauge symmetry⁴ with $\square\Lambda = 0$, the vacuum Maxwell equations

Weak-field regime

⁴After imposing the Lorenz gauge, Maxwell equations are still invariant under the gauge transformation $A^{\mu} \mapsto A^{\mu} + \partial^{\mu}\Lambda$, where Λ is any twice-differentiable scalar function .

became the wave equations

$$\square A^\mu = 0 \quad (3.28)$$

where $\square = \partial^\nu \partial_\nu$ is the D'Alembert operator. Since (3.28) is a set of homogeneous differential equations, a solution can be given as a combination of plane waves. Furthermore, since the gauge fixing spend 2 of the 4 degrees of freedom of A^μ , a solution of (3.28) is left with only 2 degrees of freedom, which are the two polarization modes.

Switching to weak-field gravity, GWs can be assumed to be small non-static perturbations of the Minkowski metric, that is

$$g_{\mu\nu} = \eta_{\mu\nu} + h_{\mu\nu} . \quad (3.29)$$

Assuming an empty spacetime, the Einstein field equations $G_{\mu\nu} = 0$ can be safely linearized in $h_{\mu\nu}$ to get

$$\square h_{\mu\nu} + \partial_\mu \partial_\nu h + 2\partial^\alpha \partial_{[\mu} h_{\nu]\alpha} = 0 . \quad (3.30)$$

As in the case of electromagnetism, these vacuum field equations have two invariances, one of which is due to the diffeomorphism invariance and can be fixed imposing the harmonic gauge $\partial^\mu h_{\mu\nu} - \frac{1}{2}\partial_\nu h = 0$, with h being the trace of $h_{\mu\nu}$. Doing so, (3.30) becomes

$$\square h_{\mu\nu} = 0 \quad (3.31)$$

which are wave equations as (3.28), and admit plane waves as solution as above. Of the original 10 degrees of freedom of $h_{\mu\nu}$, 4 has been fixed by the harmonic gauge and other 4 can be fixed with the so-called transverse-traceless gauge, leaving the plane waves with only 2 degrees of freedom which are two polarization mode, as above.

Note that the transit of a GW does not set in motion a free particle, since this would violate the equivalence principle. Instead, it can be detected as a deviation in the geodesic motion of several free particles (such as the mirrors in the Ligo/VIRGO interferometers).

From the linearized field equations in the presence of matter, we can get the wave equations

$$\square h_{\mu\nu} = -\frac{16\pi G}{c^4} T_{\mu\nu} \quad (3.32)$$

which gives the GW metric in the far-limit as

$$h^{ij}(t, \mathbf{x}) = \frac{2G}{rc^4} \ddot{Q}^{ij}(t) \Big|_{t=t_R} , \quad (3.33)$$

where

$$Q^{ij}(t) = \int x^i x^j T^{00}(t, \mathbf{x}) dV \quad (3.34)$$

is the quadrupole moment of the source, r is the distance between source and observer, and t_R is the emission time (for the full derivation see Wald 1984). Equation (3.33) shows that gravitational radiation can be emitted only by mass distributions that have at least a quadrupole moment. This can be heuristically explained by the fact that monopole radiation is prevented by the Birkhoff's theorem, dipole radiation is prevented by linear momentum conservation (since

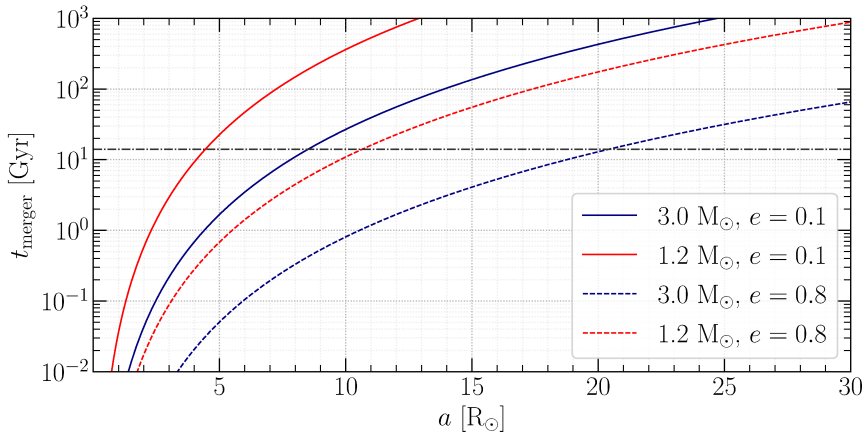


Figure 12. Merger time of a BNS according to Peters (1964). Each line represents a binary with components of equal mass, which is shown in the legend along with the eccentricity. The horizontal dash-dotted line marks $t = 14$ Gyr.

it needs the motion of the center of mass), and thus quadrupole radiation is the lowest-order radiation possible.

Outside the weak-field regime, things start to become quickly problematic for a very simple reason: Maxwell equations are linear, whether Einstein field equations are nonlinear. Indeed, the analogy with electromagnetism can bring us so far only because it relies on linearized Einstein equations. As portrayed by Sormani (2017), the proof for the existence of GWs in the fully nonlinear framework has been lacking until the beginning of 1960s. The difficulties concealing this proof have misled even Einstein himself, which had only the linearized GWs at his disposal and was never convinced about the reality of GWs. Up to date, the modelization of GWs in the strong-field regime remains a challenge for gravitational physics, but hopefully the direct detection of GWs and the characterization of their sources will provide new insights (Barack et al. 2019).

As regards binary stars, the main quadrupole radiation source is the two orbiting stars. Gravitational radiation carries away both energy and orbital angular momentum, driving a systematic spiral-in of the binary. The orbital evolution can be described averaging energy and angular momentum loss, obtaining secular equations for both the semi-major axis

$$\frac{da}{dt} = -\frac{64}{5} \frac{\mathcal{G}^3 M_1 M_2 (M_1 + M_2)}{c^5 a^3 (1 - e^2)^{7/2}} \left(1 + \frac{73}{24} e^2 + \frac{37}{96} e^4\right) \quad (3.35)$$

and eccentricity

$$\frac{de}{dt} = -\frac{304}{15} e \frac{\mathcal{G}^3 M_1 M_2 (M_1 + M_2)}{c^5 a^4 (1 - e^2)^{5/2}} \left(1 + \frac{121}{304} e^2\right) \quad (3.36)$$

as given by Peters (1964, see Figure 12)

3.1.6 Other processes

The orbital evolution of a binary star can be driven also by two other processes, namely tides and magnetic braking.

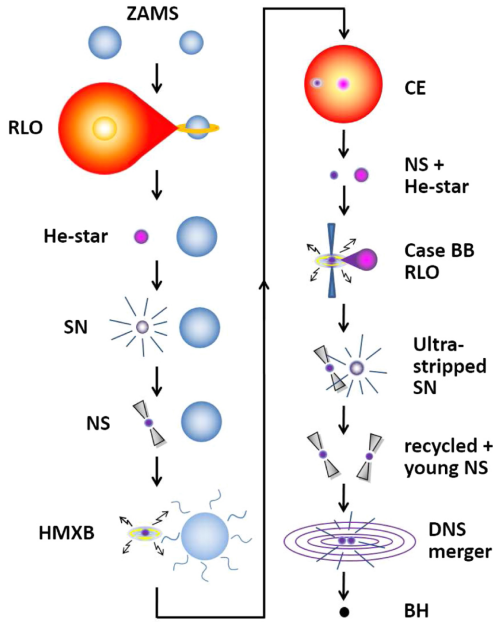


Figure 13. Main formation scenario for a merging BNS, according to Bhattacharya and van den Heuvel (1991) and Tauris and van den Heuvel (2006). There are acronyms not yet introduced, namely He-star (naked He core), HMXB (high-mass X-ray binary), and DNS (double neutron star, same as BNS). Figure from Tauris et al. (2017).

Tidal evolution

In the first, the tidal interaction between the two stars generates a spin-orbit coupling that allows the exchange of angular momentum between rotation and revolution (Hut 1981). Moreover, depending on the structure of the stellar envelope, tides dissipate energy and hence steadily evolve the orbit (Zahn 1975; Zahn 1977).

Magnetic braking

The second process is due to the coupling between stellar winds and the rotating magnetic field, in which the charged particles ejected from the star are forced to follow the rotating magnetic field lines and thus extract angular momentum. This process is thought to be efficient mainly in stars with convective envelopes, but is poorly constrained (e.g. Rappaport et al. 1983).

3.2. FORMATION SCENARIOS FOR BINARY NEUTRON STARS

After having reviewed the major processes in the evolution of a binary star, it is clear that the road leading to a close BNS could not be less straight. Indeed, the progenitors of close BNSs are likely to be born close, but the interplay of binary processes is so strong that patterns emerge when BNSs' histories are investigated.

The standard formation scenario for BNS is the one outlined by Bhattacharya and van den Heuvel (1991) and Tauris and van den Heuvel (2006) (see Figure 13). In this scenario, the progenitor is a close binary system with two massive stars. The two stars can experience several mass transfer episodes, after which the more massive star goes SN and becomes a NS. In the latest reviews of this scenario, it has been hypothesized that the progenitor of the first SN could be

stripped of its envelope, leading to a weaker kick. After a period in which the NS accretes mass through the winds of the companion, the other massive star will eventually expand and engulf the NS in a CE. If a core has been established prior to the CE, the binary composed by a NS and a stripped star may survive. At this point, the other star can be stripped even more in a case BB RLO and undergo an ultra-stripped SN (Tauris et al. 2015), or just go SN and turn into a NS. If the system survives, a BNS is born.

The previous scenario, though, can be affected by a major issue, that is the NS surviving a CE. There is a debate about whether the NS is able or not to accrete enough matter during the CE to collapse to a BH. In order to avoid this issue, another formation channel has been found, namely the “double-core” channel (Brown 1995; Dewi et al. 2006). In this scenario, the progenitor is a close binary system composed of two massive stars with a mass ratio around unity. The two stars evolve almost at the same pace, and both reach the CE phase with a well-established core. Then, if the system survives CE event and the two SNe, a BNS is born.

The need for a mass ratio near unity undermines the double-core scenario, since narrows substantially the windows for viable progenitors. Furthermore, recent hydrodynamical simulations support the idea that NSs are not able to accrete enough to collapse (MacLeod and Ramirez-Ruiz 2015) and tip the balance toward the standard scenario. Note also we should not exclude a priori other evolutionary paths besides these two, see (Tauris et al. 2017) for a review on the formation of BNSs.

After a BNS is formed, its evolution unfolds quite linearly ruled only by the GW decay. Indeed, when we look beyond the formation of a BNS, a macroscopic trend emerges: BNS form on the timescale of stellar evolution and merge on the timescale of gravitational radiation. That is to say, the BNSs’ formation happens in few Myr, while their merger might take Gyr. This has a high impact on the observational point of view because their formation can be at a very high redshift, even if the merger takes place relatively nearby.

CHAPTER 4

Synthesis of stellar populations

This Chapter exposes the numerical methods employed to simulate and explore the stellar evolution discussed in the previous Chapters. In particular, two codes are presented: the population-synthesis code SEVN with its updates, and a new code for the generation of the initial conditions of a stellar population.

4.1. THE SEVN CODE

4.1.1 Overview

The term “population synthesis” refers to the simulation of the time evolution of the stellar parameters of a given population of stars. In general, there are three tasks to be performed during the synthesis of a stellar population. First, we need to be able to simulate the evolution of every single star. Second, we need to couple the evolution of the stars in binary systems through binary processes, such as mass transfer, CE, and so on. Third, we need to create a set of initial conditions that describes every star in the population at a given moment, which will be the starting point for the simulation.

Usually, population-synthesis codes cannot rely on advanced codes (such us hydrostatic stellar evolution codes) to simulate the single stellar evolution of large populations. Instead, two simplified methods are exploited: fitting formulae or grid interpolation. In the first case, detailed stellar models are obtained with a stellar evolution code, and the desired parameters are interpolated as functions of time. The interpolated functions are then implemented in the population-synthesis code, ready to be evaluated as a star age. In the second case, the stellar parameters from the detailed stellar models are encoded in look-up tables, and the population-synthesis code interpolates the tables on-the-fly. The advantage of the second approach is its weaker bond to the stellar evolution code, so if a change in the input stellar physics is needed, then only the tables have to be replaced, without the need to change the code.

Single stellar evolution

The SEVN code is a population-synthesis code that simulates single and binary stellar evolution through grid interpolation (Spera et al. 2015; Spera and Mapelli 2017; Spera et al. 2019). The version used for this thesis is provided by default with a set of look-up tables encoding stellar evolutionary tracks from the PARSEC code (Bressan et al. 2012; Tang et al. 2014; Chen et al. 2015). These tables span a grid of masses and metallicities, the former in the interval $[2, 500] M_{\odot}$ and the later in $[10^{-4}, 4 \times 10^{-2}]$. The single tracks have been evolved from the PMS phase to either the first pulses of the TP-AGB phase or the end of the C-burning, and are provided for both ordinary stars and bare He cores. Figures 3, 4, and 5 have been obtained from these evolutionary tracks, and Figure 14 shows the HR diagram of several other tracks. A thorough description of the input physics and the implementation can be found in the papers mentioned above.

The code implements several prescriptions for core-collapse, pair-instability, and pulsational pair-instability SNe, as described in Spera et al. (2015) and Spera and Mapelli (2017). For this thesis, only two prescriptions for CCSNe have been used, namely the “delayed” and the “rapid” models from Fryer et al.

Prescriptions for SNe

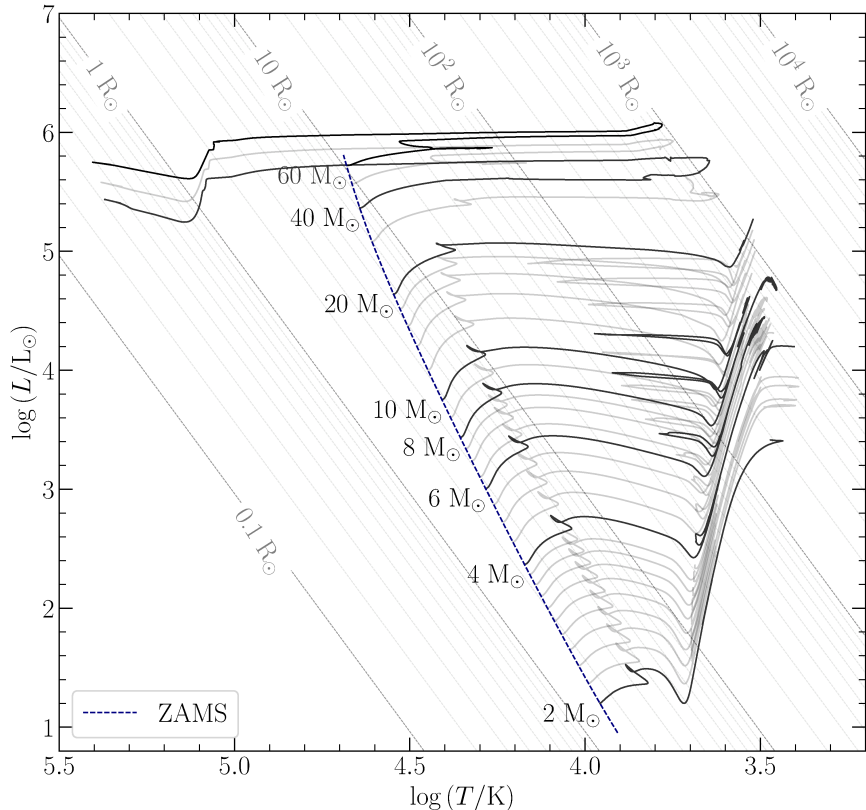


Figure 14. HR diagram of several PARSEC tracks employed in this thesis, cutted at the ZAMS. The sample span $M_{\text{ZAMS}} \in [2, 60] M_{\odot}$ at $Z = 0.02$.

(2012), with the delayed model being the default. Both these models describe CCSNe with a neutrino-driven explosion, but they differ in the instability that revives and launches the stalled shock. In the delayed model the shock is revived through the SASI, which can take up to 1 s to launch the explosion, while in the rapid model the shock is revived through the Rayleigh-Taylor instability, which instead acts in around 0.1 s. In both prescriptions the outcome of the SN is predicted from the mass of the CO core before the explosion, so they can be docked directly to the end of the PARSEC tracks.

Binary stellar evolution

The binary stellar evolution is simulated through a set of prescriptions that couples the evolution of the single stars. These prescriptions cover RLO, wind accretion, CE, kicks, tidal evolution, magnetic braking, and GW decay. Since the look-up tables are computed for non-rotating stars, the code takes into account every process that changes the spin angular momentum and follows the spin evolution using the moment of inertia as prescribed by Hurley et al. (2002). Clearly, this is not a consistent way to treat stellar rotation, but at least it allows us to simulate several binary processes in the absence of evolutionary tracks for rotating stars. A thorough description of the binary processes and their implementation is given in Spera et al. (2019).

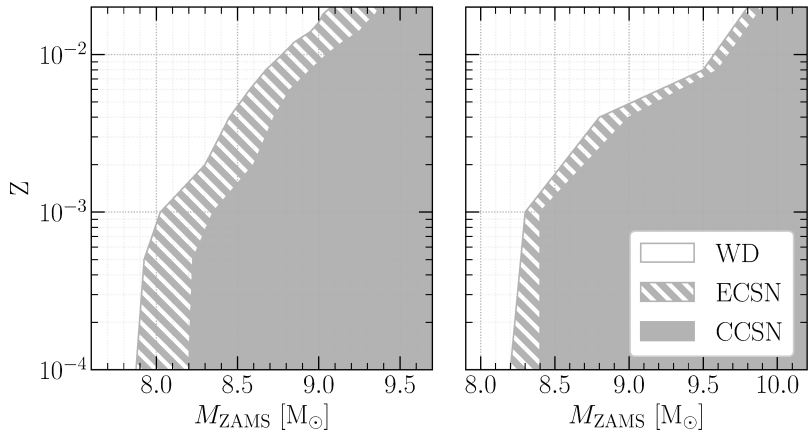


Figure 15. Fate of single stars according to the SEVN code (left) and Doherty et al. (2015, right).

4.1.2 Updates

The development of this thesis has introduced two updates in SEVN, the first being the introduction of a prescription for ECSNe. As explained above, when a star reaches the end of its evolutionary track without having grown a CO core heavier than the Chandrasekhar mass, then a CCSN cannot be triggered. When this is the case, SEVN go further and check whether the CO core has grown above the $1.37 M_{\odot}$ threshold given in Section 2.2.2. If the threshold is exceeded, then we assume the star undergoes an ECSN. The mass of the resulting NS is taken to be the mass of the CO core corrected for neutrino losses, through the formula

$$M_{\text{ns}} = \frac{\sqrt{1 + 0.3 M_{\text{CO}}} - 1}{0.075} \quad (4.1)$$

given by Timmes et al. (1996). This prescription requires the evolutionary track to end far deep into the SAGB phase, so that the mass of the CO core is close to its maximum value. The PARSEC tracks meet this requirement since they reach the TP-SAGB phase, and models show that during this phase the mass of the CO core increase of $\sim 0.01 M_{\odot}$ (Siess 2010; Doherty et al. 2015).

The second update involves the prescription for the natal kicks. With the old prescription, natal kicks were imparted with an isotropic direction and the norm sampled from a fixed Maxwell distribution. This is a common approach in population synthesis, since it is backed up by observational results such that of Hobbs et al. (2005). In this work, the proper motions of 233 Galactic pulsars are measured, and upon the selection of the 73 of them with characteristic age below 3 Myr, the probability distribution function (PDF) of natal velocities is inferred to be a Maxwell distribution with $\sigma = 265 \text{ km s}^{-1}$. As pointed out in Section 2.3.2, there are clear hints pointing toward a bimodality in the PDF, which could have a second peak at low velocities. Motivated to resolve this tension, several theoretical works propose new prescriptions able to reproduce a bimodal PDF of natal kicks. In SEVN, I have implemented the prescription proposed by Giacobbo

Electron-capture supernovae

Natal kicks

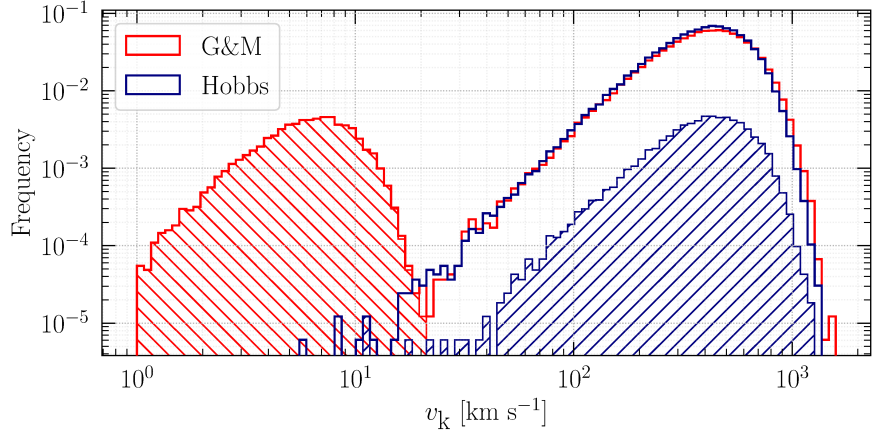


Figure 16. Natal kicks of single NSs according to the sevn code. The kicks are produced with both the prescription of Giacobbo and Mapelli (2020) (labeled as “G&M”), and a plain sampling of the PDF from Hobbs et al. (2005) (labeled as “Hobbs”). The hatched regions indicate the frequency of ECSNe only. The NSs are produced by a population of 5×10^5 stars with $Z = 0.02$ sampled from the IMF of Kroupa (2001).

and Mapelli (2020), for which

$$v_k = \frac{M_{ej}}{\langle M_{ej} \rangle} \frac{\langle M_{ns} \rangle}{M_{ns}} v_{\text{Hobbs}} \quad (4.2)$$

where $\langle M_{ns} \rangle$ and $\langle M_{ej} \rangle$ are the expected values for NSs and ejecta mass in an isolated CCSN, and v_{Hobbs} is a value sampled from the Maxwellian of Hobbs et al. This formula reproduces the effects of linear momentum conservation, as can be seen by comparing it with (2.35). In particular, in the case of CCSNe the Maxwellian of Hobbs et al. is recovered, while in the case of ECSNe or stripped SNe lower kick are produced (see Figure 16).

4.2. INITIAL CONDITIONS FOR POPULATION SYNTHESIS

As mentioned above, to synthesize a stellar population we need a set of initial conditions. These conditions must describe the population at a certain time, and they provide a starting point for the simulation. Each one of the simulations used in this thesis is initialized with a single stellar population from the ZAMS, that is to say a coeval and chemically homogeneous stellar population at its birth. The initial conditions of binary systems are produced from observational constrain through a new Python code, which I developed in collaboration with Stefano Torniamenti.

4.2.1 Masses

Each population is composed of 6×10^7 stars, whose masses are sampled from the initial mass function (IMF) of Kroupa (2001). The mass domain is taken to be $[0.5, 150]$ M_\odot , so that the Kroupa IMF reduces to

$$\mathfrak{f}(m) \propto M^{-2.3}. \quad (4.3)$$

Table 3. PDFs of mass ratios, periods, and eccentricities, from Table S3 in Sana et al. (2012).

Variable	PDF	Exponent	Domain
q	q^κ	-0.10	$[0.1, 1]$
$\log(\mathcal{P}/\text{day})$	$[\log(\mathcal{P}/\text{day})]^\pi$	-0.55	$[0.15, 5.5]^\dagger$
e	e^η	-0.45	$[0, 1)$

Notes. † While Sana et al. gives $[0.15, 3.5]$ as domain, I extend it to account for the observed large binaries (e.g. Moe and Di Stefano 2017 and references therein).

Table 4. Single, binary, higher orders fractions as a function of the stellar type, from Table 13 in Moe and Di Stefano (2017). The value of \mathcal{F}_n indicates the fraction of stars per mass bin that have n companions.

Fraction	A/late B $M_1 \in [2, 5] M_\odot$	Mid-B $M_1 \in [5, 9] M_\odot$	Early B $M_1 \in [9, 16] M_\odot$	O-type $M_1 \geq 16 M_\odot$
$\mathcal{F}_{n=0}$	0.41 ± 0.08	0.24 ± 0.08	0.16 ± 0.09	0.06 ± 0.06
$\mathcal{F}_{n=1}$	0.37 ± 0.06	0.36 ± 0.08	0.32 ± 0.10	0.21 ± 0.11
$\mathcal{F}_{n \geq 2}$	0.22 ± 0.08	0.40 ± 0.10	0.52 ± 0.13	0.73 ± 0.16

The weight of the star with mass below $0.5 M_\odot$ can be recovered by integrating the full Kroupa IMF and comparing the areas below the curve.

As has been shown by Sana et al. (2012), a large fraction of young massive stars in the local Universe belong to binary systems and binary interactions play role in their evolutions. To account for this, the code samples the initial pool of single stars and combine them to form binary systems. The assembly of binary stars is done by picking a random star, sampling the PDF of mass ratios given by Sana et al. (see Table 3), and then finding the star that best fits the mass ratio. As binaries get built, the code keeps track of the multiplicity fractions per mass bin, and the process goes on until the values given by Moe and Di Stefano (2017) are met (see Table 4). During this process the code forms also triplets, but then the wider companion is discarded and only the internal binary is kept. This is done to avoid an overestimation of the binaries. With these settings, the code ends up forming $\sim 10^6$ binaries in a population with 6×10^7 stars.

4.2.2 Orbital parameters

After the masses of single and binary stars are established, the code provides the binary systems with orbital parameters. This is done again with the PDFs given by Sana et al. (Table 3), which are consistent with the initial configurations of binaries with young massive stars. This prescription is not compatible with binaries composed only of intermediate- and low-mass stars, but this is of no concern since these systems do not interfere with the results on BNSs.

First, the eccentricity is assigned to each binary. Then, the code generates as many periods as the binaries, and it assigns them verifying that the two stars do not fill the Roche lobe. This check has a twofold effect: it avoids the immediate coalescence of the system and introduces a correlation between the various parameters of the binary. Indeed, one of the strong findings of Moe and

Masses of binary stars

Eccentricities and periods

Di Stefano is that the PDFs of mass ratios, eccentricities, and periods, are not independent, and hence the naive common approach in which the PDFs of Sana et al. are sampled separately is incorrect. This solution does not solve this issue, as it would do the direct implementations of Moe and Di Stefano results, but at least it mimics the correlation.

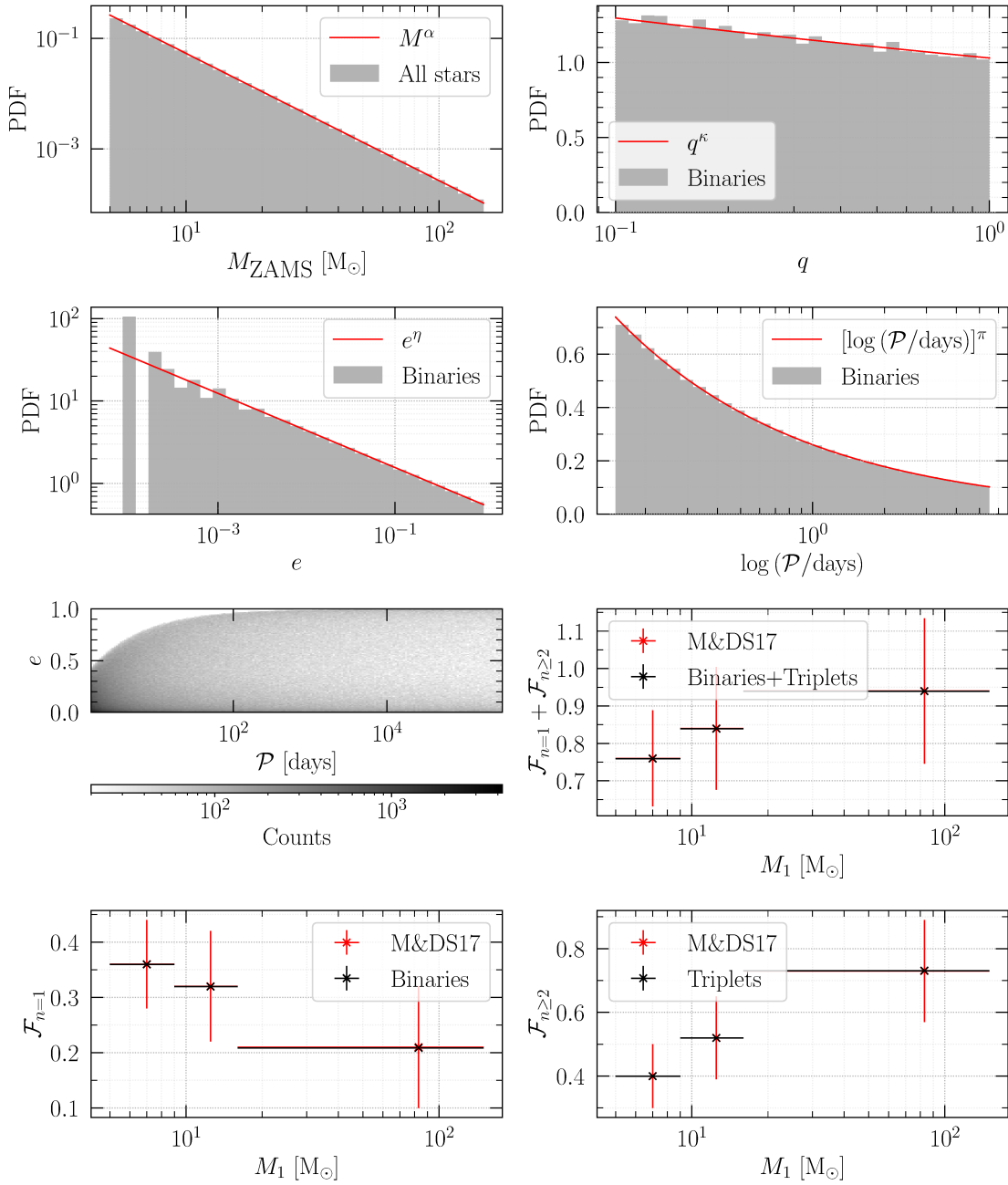


Figure 17. Initial conditions for a single simulation with $\sim 10^6$ binaries at $Z = 0.02$. In the first two rows there are the PDFs of ZAMS masses, mass ratios, eccentricities, and periods, together with their prescriptions (see Table 3). Note that the PDF of masses shows the full pool of masses above $5 M_{\odot}$, which is composed of all the single components in multiple systems plus the single stars. In the last two rows there are the initial distribution of binaries in the \mathcal{P} vs e diagram, and the total multiplicity fractions per mass bin, with their prescriptions (see Table 4). Only the binaries with the primary mass above $5 M_{\odot}$ are shown.

Results

This Chapter presents the results obtained from the simulation of various stellar populations with the methods presented above, focusing on BNSs and their progenitors. Several parameters are explored, among which metallicity, SN models, and the CE parameters. Each population starts with $\sim 10^6$ binary stars, and the fiducial model has $Z = 0.02$, CE parameters fixed to $\alpha\lambda = 0.5$, and it employs the delayed model of Fryer et al. (2012).

5.1. ECSNe AND NATAL KICKS IN BINARY STARS

If we were to consider only the ECSNe from single stars, we would find that a few percent of NSs are produced from this type of SN. This is not obvious at first, since the range of ZAMS masses leading to an ECSN is very narrow (see Figure 15), but it becomes clear as we take into account the distribution of ZAMS masses, namely the IMF. Indeed, since the IMF grows as a power law toward lower masses, and the masses of ECSN progenitors are always lighter than those of CCSN progenitors, the number of ECSN progenitors is still significant compared to that of CCSN progenitors (Doherty et al. 2015).

However, we know that massive stars belong very often to close binary systems and that they are prone to interact with the companion (Sana et al. 2012). Such interactions, like mass transfer or CE episodes, deeply shape the stellar structure and ultimately impact the growth of the stellar core. In doing so, binary interactions affect the pre-SN structure of a star and open up new paths toward ECSNe (Podsiadlowski et al. 2004).

As shown in Figure 18, the populations simulated with SEVN show this kind of behavior: the mass spectrum of ECSN progenitors broadens when binary stellar evolution is taken into account. In my simulations, this effect can only be attributed to mass transfers or CE episodes occurred during the life of a star, since the other main cause for the broadening, namely the accretion-induced collapse of a WD (Nomoto and Kondo 1991; Dessart et al. 2006), is not fully implemented yet. Another feature of Figure 18 is the lack of ECSNe above the mass spectrum for single stellar evolution, in contrast with the population synthesis of Giacobbo and Mapelli (2019). This indicates that ECSNe from lighter accreting stars are favored in my simulations.

The introduction of ECSNe in my models works together with the new momentum-conserving kicks. A variety of NSs and ejecta masses emerges from the binary stellar evolution, and this kick prescription couples it with the stochastic behavior from the Maxwellian of Hobbs et al. (2005), which is calibrated on CCSNe from isolated stars. As a consequence, the distribution of NSs' natal kicks is modulated through the properties of the SN and thus shows a complex behavior that reflects the underlying stellar evolution.

The distribution of natal kicks in binary stars is not bimodal as that from single stars, though (see Figure 19). Instead, it shows three visible peaks, two of which are clearly related to ECSNe and CCSNe, respectively. The third peak appears to be composed mainly of CCSNe, with a minor contribution from

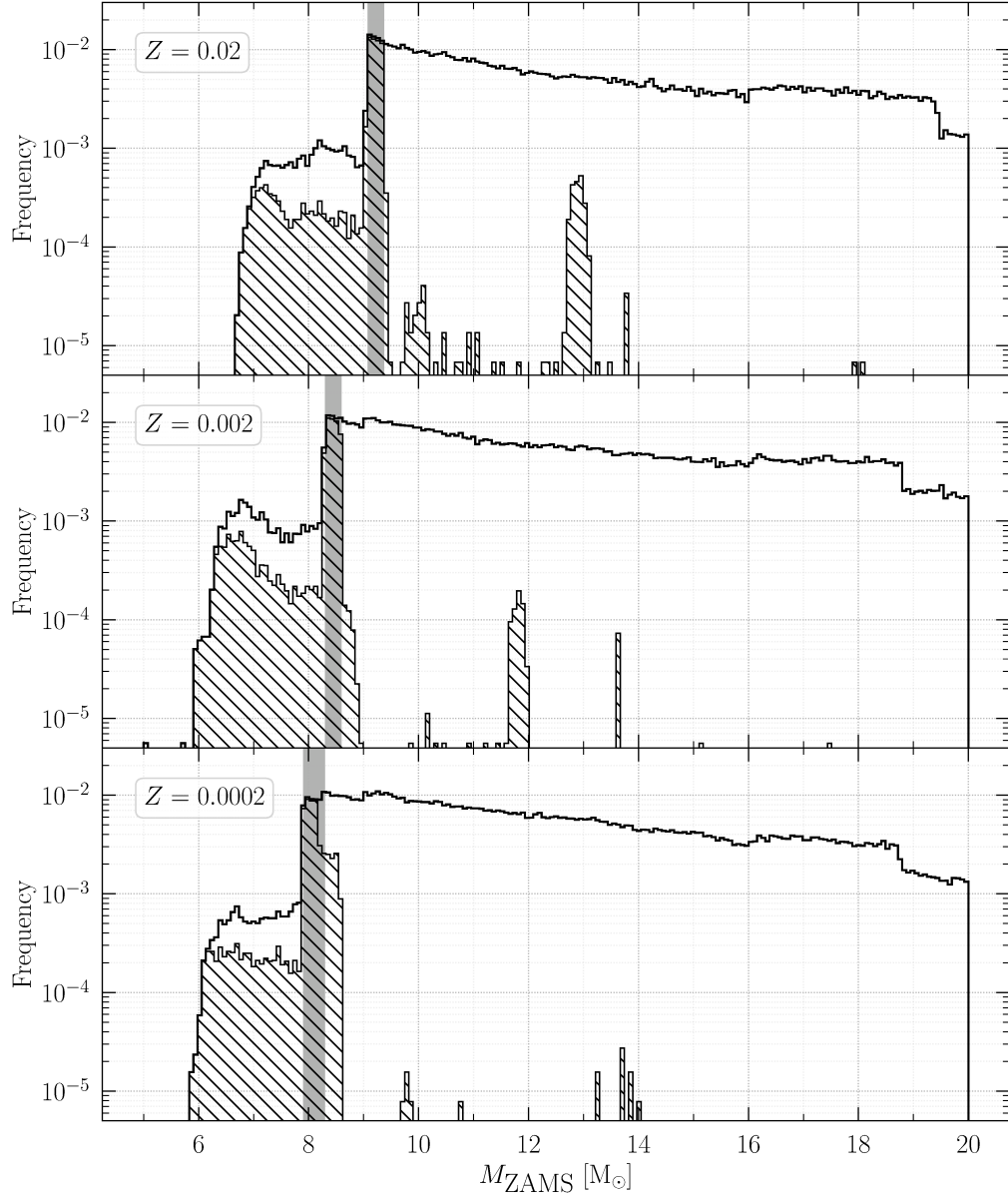


Figure 18. Distribution of the masses of NS progenitors in three different populations, according to the SEVN code. The hatched region shows the contribution of ECSNe alone. All the NSs belong to binary stars, and only ZAMS masses in the range $[5,20] M_{\odot}$ are shown to focus on the ECSN contribution. The grey strip identifies the mass spectrum of ECSN progenitors in the case of isolated single stars. The range for the mass of ECSN progenitors is widened by binary processes such as mass transfer.

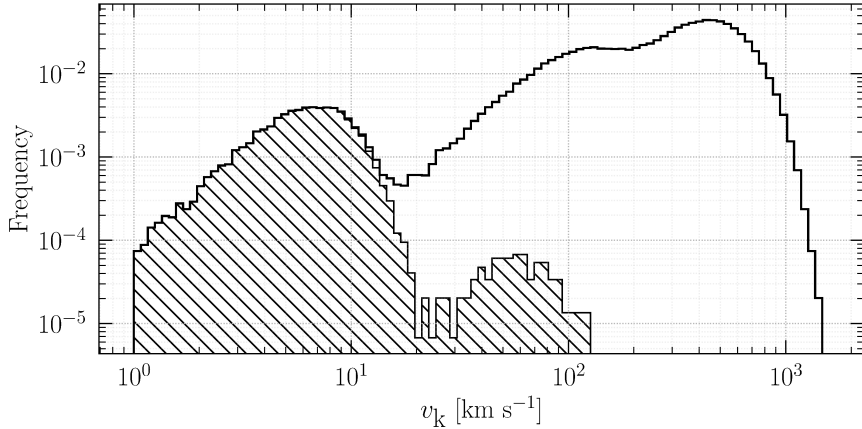


Figure 19. Distribution of NSs' natal kicks according to the SEVN code. The NSs are formed in the binary systems of a population with $Z = 0.02$, and the distribution of their natal kicks shows a complex behavior due to the interactions during the binary evolution.

ECSNe. This middle peak represents the stripped CCSNe, that are CCSNe in which part of the envelope is lost through binary interactions. As the main peak from ECSNe, this feature is a consequence of the prescription from Giacobbo and Mapelli (2020). My findings regarding natal kicks agree with that of Giacobbo and Mapelli (2019), with the difference that the secondary peak of ECSNe is less pronounced.

5.2. MASS DISTRIBUTION OF BNS PROGENITORS

Of the binary stars in my simulations, 1 every 2000 becomes a BNS. The evolutionary path that leads a binary star to become a BNS is very tight, as explained in Section 3.2, so the distributions characterizing the BNS progenitors' parameters must show some feature due to the stellar evolution. For instance, the mass distributions of the BNS progenitors do not show evident patterns in their shape, but its range shows a trend with metallicity.

I have found that the mass distributions of both the primary and the secondary component of a BNS progenitor get narrower as the metallicity decrease. Furthermore, both distributions move toward lower mass values as the metallicity decreases, which together with the previous finding means that at lower metallicities BNSs have lighter progenitors (see Figure 20).

Regarding the ECSNe, I have found that they are involved in the formation of very few BNSs ($\gtrsim 1\%$), while they seem to be very frequent in binary stars. To understand this result I have exploited a simulation with the MOBSE code (Mapelli et al. 2017; Giacobbo et al. 2018; Giacobbo and Mapelli 2018; Mapelli and Giacobbo 2018; Giacobbo, private communication), which has the same metallicity, CE prescription, and initial conditions, and I have found that also the MOBSE code gives this result. Since ECSNe results in lower kicks, they should increase the survival rate of binaries, and so they are expected to be the dominant mechanism at least for the formation of the first NS. Indeed, this strong effect

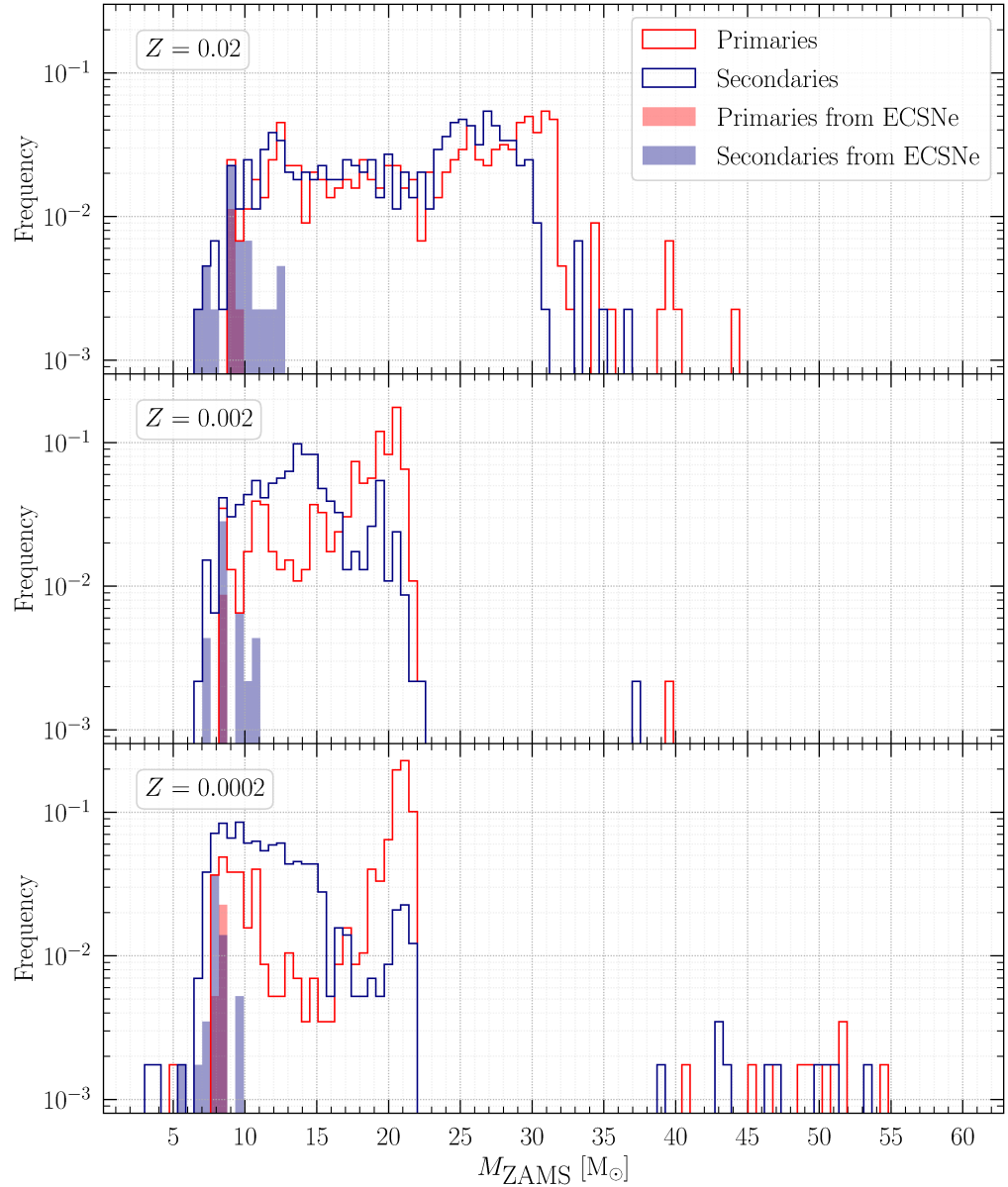


Figure 20. Distribution of the masses of BNS progenitors in three different populations, according to the SEVN code. The two binary components are shown separately, and the contribution of ECSNe alone is highlighted.

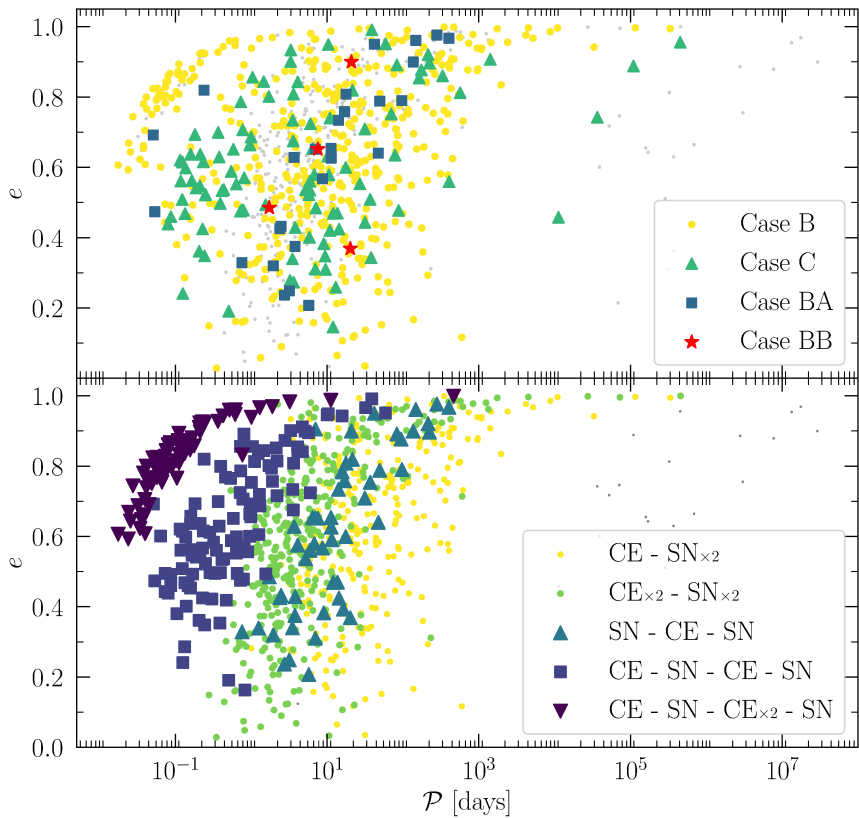


Figure 21. \mathcal{P} vs e diagram of the BNSs from a single population with the fiducial model. The diagram represents the orbital properties right after the second SN. The upper panel shows the RLO cases, while the bottom panel shows the occurrence of CE episodes.

is confirmed by other population-synthesis studies on BNSs, such as those of Giacobbo and Mapelli (2019) and Kruckow et al. (2018), which find that the majority of the first NSs are formed through ECSNe. My findings show that this result is likely due to the simulation’s setup, and so should be addressed in future studies with the SEVN code.

5.3. BNSs IN SINGLE STELLAR POPULATIONS

As shown by Figure 21, a large fraction of BNS progenitors undergo mass transfer during their life, and almost all of them go through one CE episode at least. This agrees with all the considerations made in from theoretical framework, in first place with the fact that massive binary stars are likely to interact, and in second place with the formation scenarios outlined in Section 3.2. In the upper panel of Figure 21 we can see also a few Case BB RLO, which are potential ultra-stripped SN progenitors.

From Figure 21, we can notice how the occurrence of CE episodes shows a pattern in the \mathcal{P} vs e plane (bottom panel), whether the RLO cases seems to

be randomly spread out (upper panel). The upper panel gives also a visual representation for the two formation scenarios: the dots are indeed the BNSs formed through the standard scenario, while triangles and squares are the BNSs formed through the double-core scenario. In the fiducial model, the first scenario produces 70% of the BNSs, while the second produces 27%, in agreement with the findings of Vigna-Gómez et al. (2018).

Few variations of the fiducial models have been explored. Figure 22 presents the \mathcal{P} vs e diagram of the BNSs produced by these populations, where I have highlighted the BNSs that merge within a Hubble time (hereafter merging BNSs).

The variation of Z changes both the distribution of BNSs over the diagram and the number of BNSs. While the first effect is probably related to intertwined evolutionary processes, the second effect can be linked to the shift toward lower masses of the SNe mass spectrum.

The variations in the input physics, namely the change in the SNe model and in the CE prescription, show different behaviors. The population simulated with $\alpha\lambda = 0.1$ clearly deviates from the fiducial model, whereas the population with the rapid model does not. The CE process is indeed known as one of the main uncertainties in the synthesis of binary compact objects (e.g. Dominik et al. 2012; Giacobbo and Mapelli 2018), and Figure 22 shows how severely its impact can be, both on the number and the properties of BNSs. In addition to this, my models use a fixed $\lambda\alpha$ value, while it is widely recognized that λ and α can vary depending on the stellar structure (e.g. Dewi and Tauris 2000).

5.4. BNSs FROM CONTINUOUS STAR FORMATION

In order to confront the synthetic BNSs with the Galactic BNSs in Table 2, we must evolve the synthetic populations for a time equal to the Milky Way's age and take into account its star formation history. Since this task goes far beyond the aim of this thesis, I have approximated this process simulating how each BNS population would appear after 10 Gyr of constant star formation, at a rate of $1 M_{\odot} \text{ yr}^{-1}$. To do so, I have evolved the BNSs in Figure 22 with equation (3.35) and (3.36) for 10 Gyr, then I have taken a snapshot every 100 Myr, and finally staked all the snapshots in one diagram. Since each population has an initial total mass of $\sim 10^8 M_{\odot}$, each snapshot represents a burst of star formation.

The result is shown in Figure 23, and despite its rough approach, it still makes a reasonable comparison. To understand the plot, let us recall from (3.35) and (3.36) that

$$\frac{da}{dt} \propto -\frac{1}{a^3}$$

and

$$\frac{de}{dt} \propto -\frac{1}{a^4} .$$

These relations imply that BNSs with close orbit evolve quickly through GW decay, while wider BNSs hardly evolve. Indeed, confronting Figure 22 with 23, one can see that BNSs with a period above 10 days are frozen in place, while those with periods below 0.1 days disappear right after spawning. Even if the match is not perfect, I have found that my synthetic populations are compatible with the Galactic population.

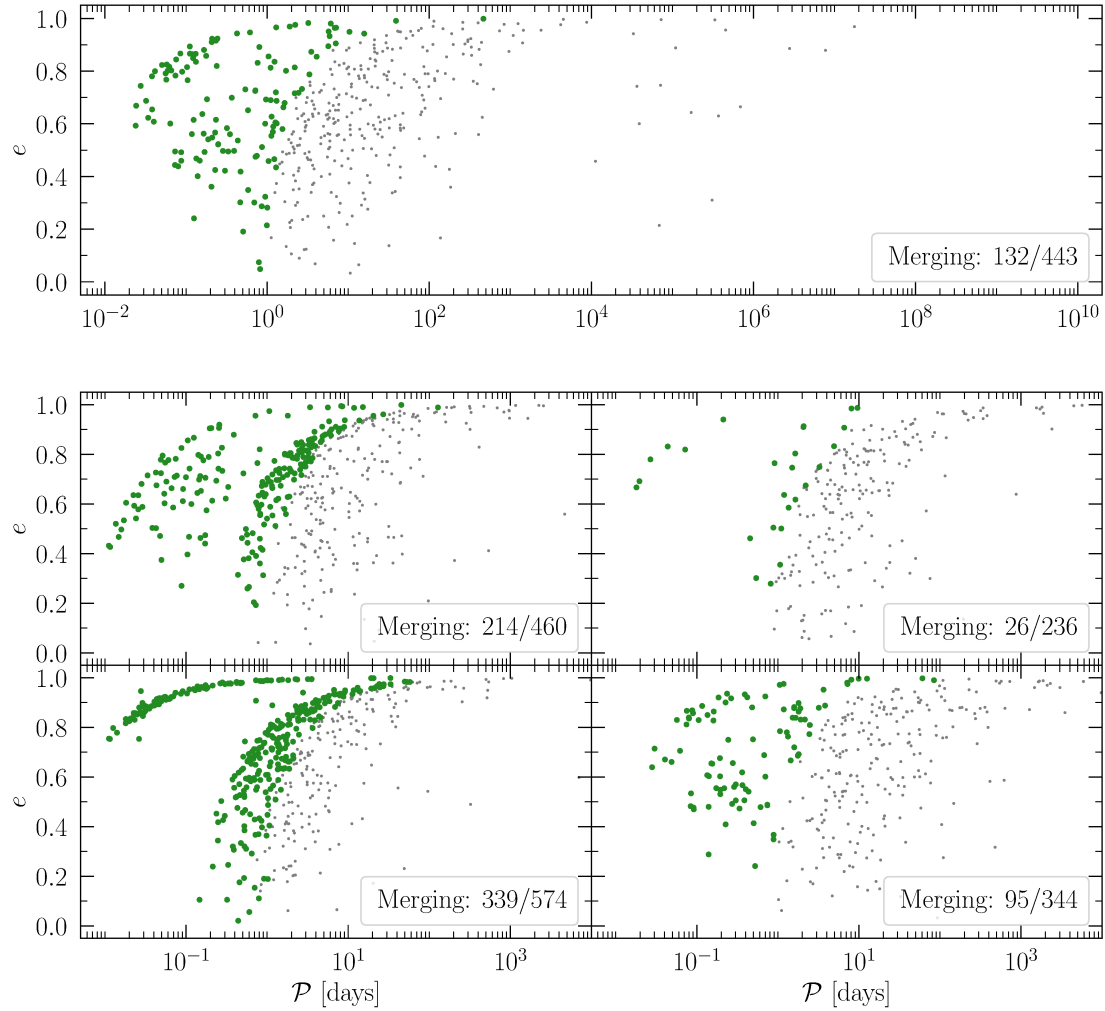


Figure 22. \mathcal{P} vs e diagram of the BNSs from several single populations, with the merging BNSs highlighted in green. The diagram represents the orbital properties right after the second SN. The upper panel shows the fiducial model, which has $Z = 0.02$. $\alpha\lambda = 0.5$, and delayed model for SNe. The bottom panels shows four variation of the fiducial model, namely $Z = 0.002$ (top left), $Z = 0.0002$ (bottom left), $\alpha\lambda = 0.1$ (top right), and rapid model for SNe (bottom right).

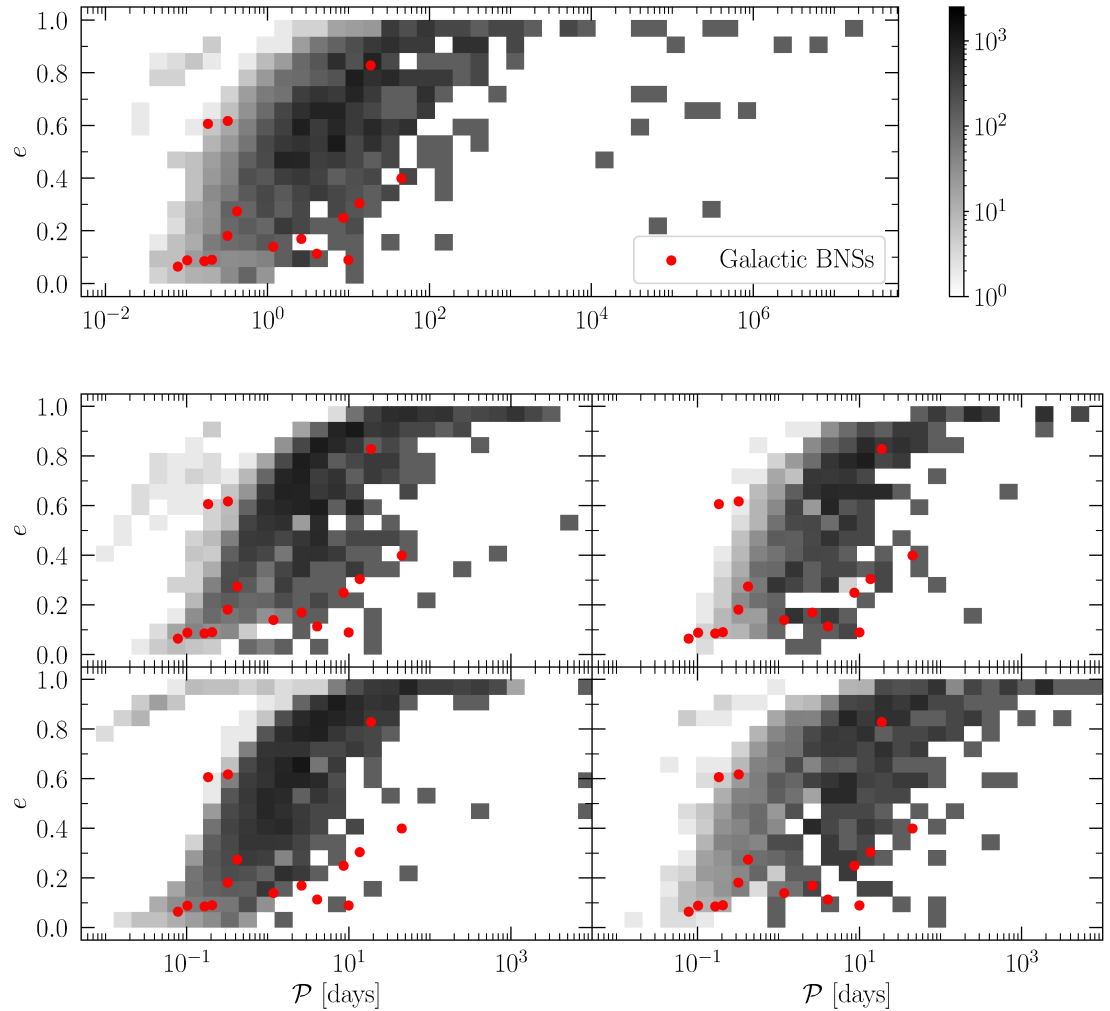


Figure 23. \mathcal{P} vs e diagram of the BNSs from several single populations, evolved with a continuous star formation as described in Section 5.3. The upper panel shows the fiducial model. The bottom panels shows four variation of the fiducial model, namely $Z = 0.002$ (top left), $Z = 0.0002$ (bottom left), $\alpha\lambda = 0.1$ (top right), and rapid model for SNe (bottom right). The red dots indicates the Galactic BNSs from Table 2.

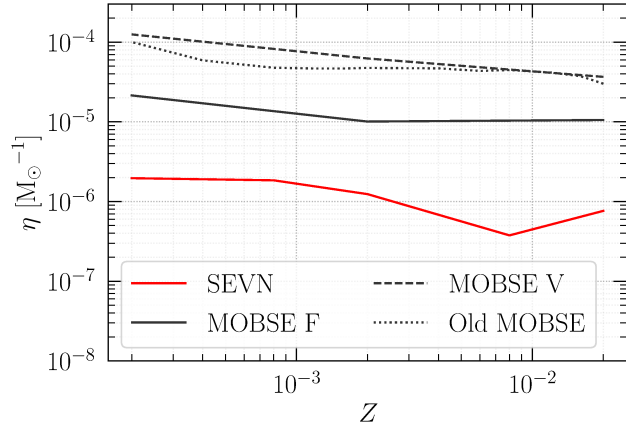


Figure 24. Merger efficiency of the fiducial model, according to the SEVN and MOBSE codes. The labels identify the simulations obtained with SEVN (SEVN), MOBSE with fixed λ (MOBSE F), MOBSE with variable λ (MOBSE V), and MOBSE with variable λ and initial conditions from Giacobbo and Mapelli (2020, Old MOBSE). See text for details.

5.5. MERGER RATE

For each synthetic population, let us define the BNS merger efficiency as

$$\eta = \frac{N_{\text{BNS}}}{M_{\text{tot}}} \quad (5.1)$$

where N_{BNS} is the number of BNSs merged in a Hubble time, and M_{tot} is the initial total mass of the stellar population. The dependence of η on the metallicity, namely $\eta(Z)$, can be estimated computing it for populations with different metallicities and then using a linear interpolation. Figure 24 shows the merger efficiency of the fiducial model, and compares the simulation from SEVN with a set of simulations from the MOBSE code (Mapelli, private communication). In general, I have found that MOBSE has an overall higher efficiency. This is caused in first approximation by the SN mass spectrum of MOBSE, which extends to masses lower than those of SEVN with PARSEC tracks, and hence increases the number of SN progenitors. The fiducial model has been simulated with MOBSE employing both a fixed hardcoded λ , and a prescription for a variable λ . The simulation with fixed λ has a merger efficiency which is higher than SEVN, but lower than MOBSE with variable λ . This result agrees with the strong impact of the CE prescription on the number of BNSs noticed in Section 5.3, and stresses the necessity of an adequate prescription for λ . I have also computed the merger efficiency from set of MOBSE's simulations employing a varying λ and the initial conditions from Giacobbo and Mapelli (2018). Figure 24 shows no difference between the two simulations with old and new initial conditions, which is in agreement with the results of de Mink and Belczynski (2015) and Klencki et al. (2018) showing that their impact on the merger efficiency is negligible.

Following Giacobbo and Mapelli (2018), the local merger rate density (MRD)

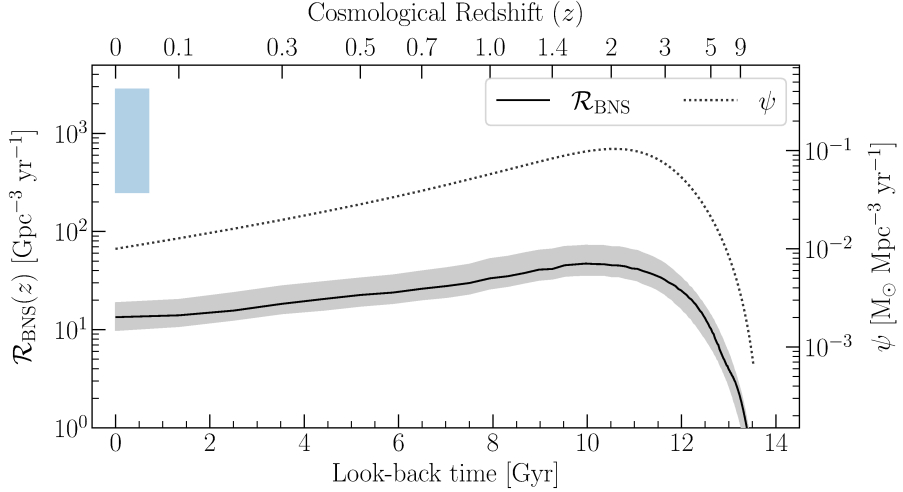


Figure 25. Cosmic MRD for the fiducial model, according to the `COSMORATE` code (Santoliquido et al. 2020). The grey area identifies the MRD’s 90% credible interval, while the light blue box identifies the 90% credible interval of the local MRD given by the LIGO/Virgo Collaboration (Abbott et al. 2020).

is given by

$$\mathcal{R}_{\text{BNS}} = \frac{1}{t_{\text{lb}}(z=0.1)} \int_{z_{\text{max}}}^0 f_{\text{loc}}(z') \psi(z') \frac{dt_{\text{lb}}}{dz'} dz' , \quad (5.2)$$

where

$$t_{\text{lb}}(z) = \frac{1}{H_0} \int_0^z \frac{1}{(1+z')[\Omega_M(1+z')^3 + \Omega_\Lambda]^{1/2}} dz' \quad (5.3)$$

is the look-back time at redshift z , $f_{\text{loc}}(z')$ is the fraction of BNS per unit solar mass that form at z' and merge at $z < 0.1$, and $\psi(z)$ is the star formation rate density given by Madau and Fragos (2017). I assume $z < 0.1$ as the local Universe and $z_{\text{max}} = 15$ as the start of star formation in the Universe. The fraction $f_{\text{loc}}(z')$ can be computed for a set of populations with different metallicities and then interpolated, through the formula

$$f_{\text{loc}}(z') = \eta(Z) \left. \frac{n_{\text{BNS}}(z', Z)}{N_{\text{BNS}}(Z)} \right|_{Z=Z(z)} \quad (5.4)$$

where $n_{\text{BNS}}(z', Z)$ is the number of BNS merging at z' , and $Z(z)$ is the average evolution of metallicity with redshift (e.g. De Cia et al. 2018). A general formulation of \mathcal{R} , which takes into account the metallicity spread into $Z(z)$ and can be used to compute the cosmic MRD, can be found in Abbott et al. (2020).

The fiducial model simulated with the `SEVN` code gives $9.9\text{--}18.7 \text{ Gpc}^{-3} \text{ yr}^{-1}$ as the 90% credible interval of the local MRD. This value is well below the LIGO/Virgo Collaboration estimate (Abbott et al. 2020), but is in line with other recent results that find the LIGO/Virgo estimate hard to match (Dominik et al. 2013; Chruslinska et al. 2018; Belczynski et al. 2018; Giacobbo and Mapelli 2018). This can be due to several causes, such as low statistics in the observational estimate, or poorly assessed formation channels. Finally, the low number of

BNSs formed with ECSNe might also play a role and deserves more investigation. To summarize, we have multiple hints indicating that the SEVN code has room for improvement, so further work is needed before we can aim to assess the nature of this last result.

CHAPTER 6

Summary and conclusions

This thesis investigates the demography of BNSs, focusing on the impact that natal kicks and ECSNe have on BNSs. I have performed the study by means of population synthesis with the SEVN code (Spera et al. 2015; Spera and Mapelli 2017; Spera et al. 2019), which I have updated to include ECSNe and a new prescription for momentum-conserving natal kicks (Giacobbo and Mapelli 2020). Since its grid-based approach to single stellar evolution, the SEVN code has been coupled to a set of stellar evolutionary tracks generated with the PARSEC code (Bressan et al. 2012; Tang et al. 2014; Chen et al. 2015). The set of initial conditions of each simulation has been produced with a new Python code based on observational constraints (Sana et al. 2012; Moe and Di Stefano 2017), which I have developed in collaboration with Stefano Torniamenti. With this setup, I have simulated the evolution of stellar populations with $\sim 10^6$ binary stars each. Each simulation was run with different parameters, such as metallicity, SN model, and CE parameters.

Regarding binary stars, I have found that the interactions between the binary's components broaden the mass spectrum of ECSN progenitors, which is otherwise very narrow (see Figure 18). Moreover, the introduction of a prescription for momentum-conserving natal kicks couples the distribution of natal velocities to the properties of the SNe. This coupling modulates the underlying observational distribution and produces a multi-peaked distribution (see Figure 19) that can relax the tension emerging from recent observational results (e.g. Hobbs et al. 2005; Verbunt et al. 2017).

Regarding progenitors of BNSs, I have found that their mass spectrum changes with the metallicity (see Figure 20). However, few of them are produced through ECSNe, contrary to what is found by other population-synthesis studies (e.g. Giacobbo and Mapelli 2019; Kruckow et al. 2018). I have also found that almost all of the progenitors go through mass transfer and CE episodes (see Figure 21), which is in agreement with observations of massive binaries such as those of Sana et al. (2012). In the fiducial model, around 70% of them become BNSs through the standard scenario (no CE prior the first SN Bhattacharya and van den Heuvel 1991; Tauris and van den Heuvel 2006), while around 27% go through the double-core scenario (Brown 1995; Dewi et al. 2006, CE can happen before the first SN).

Regarding BNSs, I have found that the uncertainties on the CE parameters have a huge impact on the outcome of population synthesis (see Figure 22), as already widely recognized (e.g. Dominik et al. 2012; Giacobbo and Mapelli 2018). The orbital properties of the fiducial population of BNSs are in a good agreement with those of Galactic BNSs when a reasonable star formation is taken into account (see Figure 23).

To assess the merger efficiency of the fiducial model, I have compared the results from the SEVN code with those from another population-synthesis code, namely the MOBSE code (Mapelli et al. 2017; Giacobbo et al. 2018; Giacobbo and Mapelli 2018; Mapelli and Giacobbo 2018). The simulations from MOBSE vary in the prescription for the CE parameter λ and the initial conditions. I have found that MOBSE has an overall higher merger efficiency (see Figure 24), which

is caused in first approximation by the lower minimum mass needed to trigger a SN, and hence a higher number of SN progenitors. In second approximation, I have found that implementing a varying λ (e.g. Dewi and Tauris 2000) can raise substantially the merger efficiency, while the uncertainties in the initial conditions do not have a great impact, as already shown by de Mink and Belczynski (2015) and Klencki et al. (2018).

The local MRD from the fiducial model simulated with SEVN is $\sim 13.6 \text{ Gpc}^{-3} \text{ yr}^{-1}$, which is well below the observational estimate of $290\text{-}2810 \text{ Gpc}^{-3} \text{ yr}^{-1}$ from the LIGO/Virgo Collaboration (Abbott et al. 2020, see Figure 25). This discrepancy can be due to several factors (e.g. low statistics effects on the observational estimate, or poorly understood formation channels) and has been already encountered by several other population-synthesis studies (Dominik et al. 2013; Chruslinska et al. 2018; Belczynski et al. 2018; Giacobbo and Mapelli 2018).

As a concluding remark, I emphasize that this thesis makes room for several future developments. Among the results obtained, the lack of BNSs formed through ECSNe and the low merger efficiency deserve further investigation, in terms of both physics and software development.

Bibliography

- Abadie, J. et al. (2010). “Predictions for the rates of compact binary coalescences observable by ground-based gravitational-wave detectors”. In: *Classical and Quantum Gravity* 27.17, p. 173001. DOI: [10.1088/0264-9381/27/17/173001](https://doi.org/10.1088/0264-9381/27/17/173001).
- Abbott, B. P. et al. (2017a). “GW170817: Observation of Gravitational Waves from a Binary Neutron Star Inspiral”. In: *Physical Review Letters* 119.16, 161101, p. 161101. DOI: [10.1103/PhysRevLett.119.161101](https://doi.org/10.1103/PhysRevLett.119.161101).
- (2017b). “Multi-messenger Observations of a Binary Neutron Star Merger”. In: *The Astrophysical Journal* 848.2, p. L12. DOI: [10.3847/2041-8213/aa91c9](https://doi.org/10.3847/2041-8213/aa91c9).
- Abbott, B. P. et al. (2020). “GW190425: Observation of a Compact Binary Coalescence with Total Mass $\sim 3.4 M_{\odot}$ ”. In: *The Astrophysical Journal Letters* 892.1, L3, p. L3. DOI: [10.3847/2041-8213/ab75f5](https://doi.org/10.3847/2041-8213/ab75f5).
- Arzoumanian, Z. et al. (2002). “The Velocity Distribution of Isolated Radio Pulsars”. In: *The Astrophysical Journal* 568.1, pp. 289–301. DOI: [10.1086/338805](https://doi.org/10.1086/338805).
- Baade, W. and F. Zwicky (1934). “Cosmic Rays from Super-novae”. In: *Proceedings of the National Academy of Science* 20.5, pp. 259–263. DOI: [10.1073/pnas.20.5.259](https://doi.org/10.1073/pnas.20.5.259).
- Barack, L. et al. (2019). “Black holes, gravitational waves and fundamental physics: a roadmap”. In: *Classical and Quantum Gravity* 36.14, p. 143001. DOI: [10.1088/1361-6382/ab0587](https://doi.org/10.1088/1361-6382/ab0587).
- Belczynski, K. et al. (2018). “The origin of the first neutron star - neutron star merger”. In: *Astronomy & Astrophysics* 615, A91. DOI: [10.1051/0004-6361/201732428](https://doi.org/10.1051/0004-6361/201732428).
- Beniamini, P. and T. Piran (2016). “Formation of double neutron star systems as implied by observations”. In: *Monthly Notices of the Royal Astronomical Society* 456.4, pp. 4089–4099. DOI: [10.1093/mnras/stv2903](https://doi.org/10.1093/mnras/stv2903).
- Berger, E. (2014). “Short-Duration Gamma-Ray Bursts”. In: *Annual Review of Astronomy and Astrophysics* 52, pp. 43–105. DOI: [10.1146/annurev-astro-081913-035926](https://doi.org/10.1146/annurev-astro-081913-035926).
- Bhattacharya, D. and E. P. J. van den Heuvel (1991). “Formation and evolution of binary and millisecond radio pulsars”. In: *Physics Reports* 203.1-2, pp. 1–124. DOI: [10.1016/0370-1573\(91\)90064-S](https://doi.org/10.1016/0370-1573(91)90064-S).
- Blaauw, A. (1961). “On the origin of the O- and B-type stars with high velocities (the “run-away” stars), and some related problems”. In: *Bulletin of the Astronomical Institutes of the Netherlands* 15, p. 265.
- Boersma, J. (1961). “Mathematical theory of the two-body problem with one of the masses decreasing with time”. In: *Bulletin of the Astronomical Institutes of the Netherlands* 15, pp. 291–301.

- Bressan, A. et al. (2012). “PARSEC: stellar tracks and isochrones with the PAdova and TRieste Stellar Evolution Code”. In: *Monthly Notices of the Royal Astronomical Society* 427.1, pp. 127–145. DOI: [10.1111/j.1365-2966.2012.21948.x](https://doi.org/10.1111/j.1365-2966.2012.21948.x).
- Brown, G. E. (1995). “Neutron Star Accretion and Binary Pulsar Formation”. In: *The Astrophysical Journal* 440, p. 270. DOI: [10.1086/175268](https://doi.org/10.1086/175268).
- Cameron, A. D. et al. (2018). “The High Time Resolution Universe Pulsar Survey - XIII. PSR J1757-1854, the most accelerated binary pulsar”. In: *Monthly Notices of the Royal Astronomical Society* 475.1, pp. L57–L61. DOI: [10.1093/mnrasl/sly003](https://doi.org/10.1093/mnrasl/sly003).
- Champion, D. J. et al. (2004). “PSR J1829+2456: a relativistic binary pulsar”. In: *Monthly Notices of the Royal Astronomical Society* 350.4, pp. L61–L65. DOI: [10.1111/j.1365-2966.2004.07862.x](https://doi.org/10.1111/j.1365-2966.2004.07862.x).
- Chen, Y. et al. (2015). “PARSEC evolutionary tracks of massive stars up to $350 M_{\odot}$ at metallicities $0.0001 \leq Z \leq 0.04$ ”. In: *Monthly Notices of the Royal Astronomical Society* 452.1, pp. 1068–1080. DOI: [10.1093/mnras/stv1281](https://doi.org/10.1093/mnras/stv1281).
- Chiosi, C. (1998). “Fundamentals of Stellar Evolution Theory: Understanding the HRD”. In: *Stellar astrophysics for the local group*. Cambridge Contemporary Astrophysics. Cambridge University Press, p. 1.
- Chruslinska, M. et al. (2018). “Double neutron stars: merger rates revisited”. In: *Monthly Notices of the Royal Astronomical Society* 474.3, pp. 2937–2958. DOI: [10.1093/mnras/stx2923](https://doi.org/10.1093/mnras/stx2923).
- Corongiu, A. et al. (2007). “The binary pulsar PSR J1811-1736: evidence of a low amplitude supernova kick”. In: *Astronomy & Astrophysics* 462.2, pp. 703–709. DOI: [10.1051/0004-6361:20054385](https://doi.org/10.1051/0004-6361:20054385).
- De Cia, A. et al. (2018). “The cosmic evolution of dust-corrected metallicity in the neutral gas”. In: *Astronomy & Astrophysics* 611, A76. DOI: [10.1051/0004-6361/201731970](https://doi.org/10.1051/0004-6361/201731970).
- de Mink, S. E. and K. Belczynski (2015). “Merger Rates of Double Neutron Stars and Stellar Origin Black Holes: The Impact of Initial Conditions on Binary Evolution Predictions”. In: *The Astrophysical Journal* 814.1, p. 58. DOI: [10.1088/0004-637X/814/1/58](https://doi.org/10.1088/0004-637X/814/1/58).
- Dessart, L. et al. (2006). “Multidimensional Simulations of the Accretion-induced Collapse of White Dwarfs to Neutron Stars”. In: *The Astrophysical Journal* 644.2, pp. 1063–1084. DOI: [10.1086/503626](https://doi.org/10.1086/503626).
- Dewi, J. D. M. and T. M. Tauris (2000). “On the energy equation and efficiency parameter of the common envelope evolution”. In: *Astronomy & Astrophysics* 360, pp. 1043–1051.
- Dewi, J. D. M. et al. (2006). “Double-core evolution and the formation of neutron star binaries with compact companions”. In: *Monthly Notices of the Royal Astronomical Society* 368.4, pp. 1742–1748. DOI: [10.1111/j.1365-2966.2006.10233.x](https://doi.org/10.1111/j.1365-2966.2006.10233.x).
- Doherty, C. L. et al. (2015). “Super- and massive AGB stars - IV. Final fates - initial-to-final mass relation”. In: *Monthly Notices of the Royal Astronomical Society* 446.3, pp. 2599–2612. DOI: [10.1093/mnras/stu2180](https://doi.org/10.1093/mnras/stu2180).
- Doherty, C. L. et al. (2017). “Super-AGB Stars and their Role as Electron Capture Supernova Progenitors”. In: *Publications of the Astronomical Society of Australia* 34, e056. DOI: [10.1017/pasa.2017.52](https://doi.org/10.1017/pasa.2017.52).

- Dominik, M. et al. (2012). "Double Compact Objects. I. The Significance of the Common Envelope on Merger Rates". In: *The Astrophysical Journal* 759.1, p. 52. DOI: [10.1088/0004-637X/759/1/52](https://doi.org/10.1088/0004-637X/759/1/52).
- Dominik, M. et al. (2013). "Double Compact Objects. II. Cosmological Merger Rates". In: *The Astrophysical Journal* 779.1, p. 72. DOI: [10.1088/0004-637X/779/1/72](https://doi.org/10.1088/0004-637X/779/1/72).
- Eggleton, P. P. (1983). "Aproximations to the radii of Roche lobes." In: *The Astrophysical Journal* 268, pp. 368–369. DOI: [10.1086/160960](https://doi.org/10.1086/160960).
- Faulkner, A. J. et al. (2005). "PSR J1756-2251: A New Relativistic Double Neutron Star System". In: *The Astrophysical Journal Letters* 618.2, pp. L119–L122. DOI: [10.1086/427776](https://doi.org/10.1086/427776).
- Fonseca, E. et al. (2014). "A Comprehensive Study of Relativistic Gravity Using PSR B1534+12". In: *The Astrophysical Journal* 787.1, p. 82. DOI: [10.1088/0004-637X/787/1/82](https://doi.org/10.1088/0004-637X/787/1/82).
- Fryer, C. L. and V. Kalogera (1997). "Double Neutron Star Systems and Natal Neutron Star Kicks". In: *The Astrophysical Journal* 489.1, pp. 244–253. DOI: [10.1086/304772](https://doi.org/10.1086/304772).
- Fryer, C. L. et al. (2012). "Compact Remnant Mass Function: Dependence on the Explosion Mechanism and Metallicity". In: *The Astrophysical Journal* 749.1, p. 91. DOI: [10.1088/0004-637X/749/1/91](https://doi.org/10.1088/0004-637X/749/1/91).
- Giacconi, R. et al. (1962). "Evidence for x Rays From Sources Outside the Solar System". In: *Physical Review Letters* 9.11, pp. 439–443. DOI: [10.1103/PhysRevLett.9.439](https://doi.org/10.1103/PhysRevLett.9.439).
- Giacobbo, N. and M. Mapelli (2018). "The progenitors of compact-object binaries: impact of metallicity, common envelope and natal kicks". In: *Monthly Notices of the Royal Astronomical Society* 480.2, pp. 2011–2030. DOI: [10.1093/mnras/sty1999](https://doi.org/10.1093/mnras/sty1999).
- (2019). "The impact of electron-capture supernovae on merging double neutron stars". In: *Monthly Notices of the Royal Astronomical Society* 482.2, pp. 2234–2243. DOI: [10.1093/mnras/sty2848](https://doi.org/10.1093/mnras/sty2848).
- (2020). "Revising Natal Kick Prescriptions in Population Synthesis Simulations". In: *The Astrophysical Journal* 891.2, p. 141. DOI: [10.3847/1538-4357/ab7335](https://doi.org/10.3847/1538-4357/ab7335).
- Giacobbo, N. et al. (2018). "Merging black hole binaries: the effects of progenitor's metallicity, mass-loss rate and Eddington factor". In: *Monthly Notices of the Royal Astronomical Society* 474.3, pp. 2959–2974. DOI: [10.1093/mnras/stx2933](https://doi.org/10.1093/mnras/stx2933).
- Hewish, A. et al. (1968). "Observation of a Rapidly Pulsating Radio Source". In: *Nature* 217.5130, pp. 709–713. DOI: [10.1038/217709a0](https://doi.org/10.1038/217709a0).
- Hobbs, G. et al. (2005). "A statistical study of 233 pulsar proper motions". In: *Monthly Notices of the Royal Astronomical Society* 360.3, pp. 974–992. DOI: [10.1111/j.1365-2966.2005.09087.x](https://doi.org/10.1111/j.1365-2966.2005.09087.x).
- Hulse, R. A. and J. H. Taylor (1975). "Discovery of a pulsar in a binary system." In: *The Astrophysical Journal Letters* 195, pp. L51–L53. DOI: [10.1086/181708](https://doi.org/10.1086/181708).
- Hurley, J. R. et al. (2002). "Evolution of binary stars and the effect of tides on binary populations". In: *Monthly Notices of the Royal Astronomical Society* 329.4, pp. 897–928. DOI: [10.1046/j.1365-8711.2002.05038.x](https://doi.org/10.1046/j.1365-8711.2002.05038.x).
- Hut, P. (1981). "Tidal evolution in close binary systems." In: *Astronomy & Astrophysics* 99, pp. 126–140.

- Ivanova, N. et al. (2013). “Common envelope evolution: where we stand and how we can move forward”. In: *The Astronomy and Astrophysics Review* 21, p. 59. DOI: [10.1007/s00159-013-0059-2](https://doi.org/10.1007/s00159-013-0059-2).
- Jacoby, B. A. et al. (2006). “Measurement of Orbital Decay in the Double Neutron Star Binary PSR B2127+11C”. In: *The Astrophysical Journal Letters* 644.2, pp. L113–L116. DOI: [10.1086/505742](https://doi.org/10.1086/505742).
- Janka, H. -T. (2012). “Explosion Mechanisms of Core-Collapse Supernovae”. In: *Annual Review of Nuclear and Particle Science* 62.1, pp. 407–451. DOI: [10.1146/annurev-nucl-102711-094901](https://doi.org/10.1146/annurev-nucl-102711-094901).
- Janssen, G. H. et al. (2008). “Multi-telescope timing of PSR J1518+4904”. In: *Astronomy & Astrophysics* 490.2, pp. 753–761. DOI: [10.1051/0004-6361:200810076](https://doi.org/10.1051/0004-6361:200810076).
- Jones, S. et al. (2016). “Do electron-capture supernovae make neutron stars?. First multidimensional hydrodynamic simulations of the oxygen deflagration”. In: *Astronomy & Astrophysics* 593, A72. DOI: [10.1051/0004-6361/201628321](https://doi.org/10.1051/0004-6361/201628321).
- Kalogera, V. et al. (2004). “The Cosmic Coalescence Rates for Double Neutron Star Binaries”. In: *The Astrophysical Journal Letters* 601.2, pp. L179–L182. DOI: [10.1086/382155](https://doi.org/10.1086/382155).
- Keith, M. J. et al. (2009). “PSR J1753-2240: a mildly recycled pulsar in an eccentric binary system”. In: *Monthly Notices of the Royal Astronomical Society* 393.2, pp. 623–627. DOI: [10.1111/j.1365-2966.2008.14234.x](https://doi.org/10.1111/j.1365-2966.2008.14234.x).
- Kippenhahn, R. et al. (2012). *Stellar Structure and Evolution*. Astronomy and Astrophysics Library. Springer-Verlag Berlin Heidelberg. DOI: [10.1007/978-3-642-30304-3](https://doi.org/10.1007/978-3-642-30304-3).
- Klencki, J. et al. (2018). “Impact of inter-correlated initial binary parameters on double black hole and neutron star mergers”. In: *Astronomy & Astrophysics* 619, A77. DOI: [10.1051/0004-6361/201833025](https://doi.org/10.1051/0004-6361/201833025).
- Knigge, C. et al. (2011). “Two populations of X-ray pulsars produced by two types of supernova”. In: *Nature* 479.7373, pp. 372–375. DOI: [10.1038/nature10529](https://doi.org/10.1038/nature10529).
- Kramer, M. et al. (2006). “Tests of General Relativity from Timing the Double Pulsar”. In: *Science* 314.5796, pp. 97–102. DOI: [10.1126/science.1132305](https://doi.org/10.1126/science.1132305).
- Kroupa, P. (2001). “On the variation of the initial mass function”. In: *Monthly Notices of the Royal Astronomical Society* 322.2, pp. 231–246. DOI: [10.1046/j.1365-8711.2001.04022.x](https://doi.org/10.1046/j.1365-8711.2001.04022.x).
- Kruckow, M. U. et al. (2018). “Progenitors of gravitational wave mergers: binary evolution with the stellar grid-based code COMBINE”. In: *Monthly Notices of the Royal Astronomical Society* 481.2, pp. 1908–1949. DOI: [10.1093/mnras/sty2190](https://doi.org/10.1093/mnras/sty2190).
- Lazarus, P. et al. (2016). “Einstein@Home Discovery of a Double Neutron Star Binary in the PALFA Survey”. In: *The Astrophysical Journal* 831.2, p. 150. DOI: [10.3847/0004-637X/831/2/150](https://doi.org/10.3847/0004-637X/831/2/150).
- Lynch, R. S. et al. (2012). “The Timing of Nine Globular Cluster Pulsars”. In: *The Astrophysical Journal* 745.2, p. 109. DOI: [10.1088/0004-637X/745/2/109](https://doi.org/10.1088/0004-637X/745/2/109).
- Lyne, A. G. and D. R. Lorimer (1994). “High birth velocities of radio pulsars”. In: *Nature* 369.6476, pp. 127–129. DOI: [10.1038/369127a0](https://doi.org/10.1038/369127a0).
- MacLeod, M. and E. Ramirez-Ruiz (2015). “Asymmetric Accretion Flows within a Common Envelope”. In: *The Astrophysical Journal* 803.1, p. 41. DOI: [10.1088/0004-637X/803/1/41](https://doi.org/10.1088/0004-637X/803/1/41).

- Madau, P. and T. Fragos (2017). “Radiation Backgrounds at Cosmic Dawn: X-Rays from Compact Binaries”. In: *The Astrophysical Journal* 840.1, p. 39. DOI: [10.3847/1538-4357/aa6af9](https://doi.org/10.3847/1538-4357/aa6af9).
- Manchester, R. N. et al. (2005). “The Australia Telescope National Facility Pulsar Catalogue”. In: *The Astronomical Journal* 129.4, pp. 1993–2006. DOI: [10.1086/428488](https://doi.org/10.1086/428488).
- Mapelli, M. and N. Giacobbo (2018). “The cosmic merger rate of neutron stars and black holes”. In: *Monthly Notices of the Royal Astronomical Society* 479.4, pp. 4391–4398. DOI: [10.1093/mnras/sty1613](https://doi.org/10.1093/mnras/sty1613).
- Mapelli, M. et al. (2017). “The cosmic merger rate of stellar black hole binaries from the Illustris simulation”. In: *Monthly Notices of the Royal Astronomical Society* 472.2, pp. 2422–2435. DOI: [10.1093/mnras/stx2123](https://doi.org/10.1093/mnras/stx2123).
- Martinez, J. G. et al. (2015). “Pulsar J0453+1559: A Double Neutron Star System with a Large Mass Asymmetry”. In: *The Astrophysical Journal* 812.2, p. 143. DOI: [10.1088/0004-637X/812/2/143](https://doi.org/10.1088/0004-637X/812/2/143).
- Martinez, J. G. et al. (2017). “Pulsar J1411+2551: A Low-mass Double Neutron Star System”. In: *The Astrophysical Journal Letters* 851.2, p. L29. DOI: [10.3847/2041-8213/aa9d87](https://doi.org/10.3847/2041-8213/aa9d87).
- Metzger, B. D. (2019). “Kilonovae”. In: *Living Reviews in Relativity* 23.1, 1, p. 1. DOI: [10.1007/s41114-019-0024-0](https://doi.org/10.1007/s41114-019-0024-0).
- Miyaji, S. et al. (1980). “Supernova triggered by electron captures.” In: *Publications of the Astronomical Society of Japan* 32, pp. 303–329.
- Moe, M. and R. Di Stefano (2017). “Mind Your Ps and Qs: The Interrelation between Period (P) and Mass-ratio (Q) Distributions of Binary Stars”. In: *The Astrophysical Journal Supplement Series* 230.2, p. 15. DOI: [10.3847/1538-4365/aa6fb6](https://doi.org/10.3847/1538-4365/aa6fb6).
- Ng, C. et al. (2018). “PSR J1755-2550: a young radio pulsar with a massive, compact companion”. In: *Monthly Notices of the Royal Astronomical Society* 476.4, pp. 4315–4326. DOI: [10.1093/mnras/sty482](https://doi.org/10.1093/mnras/sty482).
- Nomoto, K. (1984). “Evolution of 8–10 M_{\odot} stars toward electron capture supernovae. I - Formation of electron-degenerate O + NE + MG cores.” In: *The Astrophysical Journal* 277, pp. 791–805. DOI: [10.1086/161749](https://doi.org/10.1086/161749).
- (1987). “Evolution of 8–10 M_{\odot} Stars toward Electron Capture Supernovae. II. Collapse of an O + NE + MG Core”. In: *The Astrophysical Journal* 322, p. 206. DOI: [10.1086/165716](https://doi.org/10.1086/165716).
- Nomoto, K. and Y. Kondo (1991). “Conditions for Accretion-induced Collapse of White Dwarfs”. In: *The Astrophysical Journal Letters* 367, p. L19. DOI: [10.1086/185922](https://doi.org/10.1086/185922).
- Oppenheimer, J. R. and G. M. Volkoff (1939). “On Massive Neutron Cores”. In: *Physical Review* 55.4, pp. 374–381. DOI: [10.1103/PhysRev.55.374](https://doi.org/10.1103/PhysRev.55.374).
- Özel, F. and P. Freire (2016). “Masses, Radii, and the Equation of State of Neutron Stars”. In: *Annual Review of Astronomy and Astrophysics* 54, pp. 401–440. DOI: [10.1146/annurev-astro-081915-023322](https://doi.org/10.1146/annurev-astro-081915-023322).
- Paczynski, B. (1976). “Common Envelope Binaries”. In: *Structure and Evolution of Close Binary Systems*. Vol. 73. IAU Symposium, p. 75.
- Peters, P. C. (1964). “Gravitational Radiation and the Motion of Two Point Masses”. In: *Physical Review* 136.4B, pp. 1224–1232. DOI: [10.1103/PhysRev.136.B1224](https://doi.org/10.1103/PhysRev.136.B1224).

- Pfahl, E. et al. (2002). “A New Class of High-Mass X-Ray Binaries: Implications for Core Collapse and Neutron Star Recoil”. In: *The Astrophysical Journal* 574.1, pp. 364–376. DOI: [10.1086/340794](https://doi.org/10.1086/340794).
- Podsiadlowski, P. et al. (2004). “The Effects of Binary Evolution on the Dynamics of Core Collapse and Neutron Star Kicks”. In: *The Astrophysical Journal* 612.2, pp. 1044–1051. DOI: [10.1086/421713](https://doi.org/10.1086/421713).
- Poelarends, A. J. T. et al. (2008). “The Supernova Channel of Super-AGB Stars”. In: *The Astrophysical Journal* 675.1, pp. 614–625. DOI: [10.1086/520872](https://doi.org/10.1086/520872).
- Pols, O. (2011). *Binary stars*. Lecture notes. Utrecht University.
- Rappaport, S. et al. (1983). “A new technique for calculations of binary stellar evolution application to magnetic braking.” In: *The Astrophysical Journal* 275, pp. 713–731. DOI: [10.1086/161569](https://doi.org/10.1086/161569).
- Sadowski, A. et al. (2008). “The Total Merger Rate of Compact Object Binaries in the Local Universe”. In: *The Astrophysical Journal* 676.2, pp. 1162–1169. DOI: [10.1086/528932](https://doi.org/10.1086/528932).
- Sana, H. et al. (2012). “Binary Interaction Dominates the Evolution of Massive Stars”. In: *Science* 337.6093, p. 444. DOI: [10.1126/science.1223344](https://doi.org/10.1126/science.1223344).
- Santoliquido, F. et al. (2020). “The Cosmic Merger Rate Density Evolution of Compact Binaries Formed in Young Star Clusters and in Isolated Binaries”. In: *The Astrophysical Journal* 898.2, p. 152. DOI: [10.3847/1538-4357/ab9b78](https://doi.org/10.3847/1538-4357/ab9b78).
- Scheck, L. et al. (2006). “Multidimensional supernova simulations with approximative neutrino transport. I. Neutron star kicks and the anisotropy of neutrino-driven explosions in two spatial dimensions”. In: *Astronomy & Astrophysics* 457.3, pp. 963–986. DOI: [10.1051/0004-6361:20064855](https://doi.org/10.1051/0004-6361:20064855).
- Schinzel, F. K. et al. (2019). “The Tail of PSR J0002+6216 and the Supernova Remnant CTB 1”. In: *The Astrophysical Journal Letters* 876.1, p. L17. DOI: [10.3847/2041-8213/ab18f7](https://doi.org/10.3847/2041-8213/ab18f7).
- Shapiro, S. L. and S. A. Teukolsky (1983). *Black holes, white dwarfs, and neutron stars : the physics of compact objects*. Wiley-VCH. DOI: [10.1063/1.2915325](https://doi.org/10.1063/1.2915325).
- Siess, L. (2006). “Evolution of massive AGB stars. I. Carbon burning phase”. In: *Astronomy & Astrophysics* 448.2, pp. 717–729. DOI: [10.1051/0004-6361:20053043](https://doi.org/10.1051/0004-6361:20053043).
- (2007). “Evolution of massive AGB stars. II. model properties at non-solar metallicity and the fate of Super-AGB stars”. In: *Astronomy & Astrophysics* 476.2, pp. 893–909. DOI: [10.1051/0004-6361:20078132](https://doi.org/10.1051/0004-6361:20078132).
 - (2010). “Evolution of massive AGB stars. III. the thermally pulsing super-AGB phase”. In: *Astronomy & Astrophysics* 512, A10. DOI: [10.1051/0004-6361/200913556](https://doi.org/10.1051/0004-6361/200913556).
- Sormani, C. (2017). “A Two-Part Feature: The Mathematics of Gravitational Waves”. In: *Notices of the American Mathematical Society* 64, pp. 684–685. DOI: [10.1090/noti1551](https://doi.org/10.1090/noti1551).
- Spera, M. and M. Mapelli (2017). “Very massive stars, pair-instability supernovae and intermediate-mass black holes with the sevn code”. In: *Monthly Notices of the Royal Astronomical Society* 470.4, pp. 4739–4749. DOI: [10.1093/mnras/stx1576](https://doi.org/10.1093/mnras/stx1576).
- Spera, M. et al. (2015). “The mass spectrum of compact remnants from the PARSEC stellar evolution tracks”. In: *Monthly Notices of the Royal Astronomical Society* 451.4, pp. 4086–4103. DOI: [10.1093/mnras/stv1161](https://doi.org/10.1093/mnras/stv1161).

- Spera, M. et al. (2019). “Merging black hole binaries with the SEVN code”. In: *Monthly Notices of the Royal Astronomical Society* 485.1, pp. 889–907. DOI: [10.1093/mnras/stz359](https://doi.org/10.1093/mnras/stz359).
- Stovall, K. et al. (2018). “PALFA Discovery of a Highly Relativistic Double Neutron Star Binary”. In: *The Astrophysical Journal Letters* 854.2, p. L22. DOI: [10.3847/2041-8213/aaad06](https://doi.org/10.3847/2041-8213/aaad06).
- Swiggum, J. K. et al. (2015). “PSR J1930-1852: a Pulsar in the Widest Known Orbit around Another Neutron Star”. In: *The Astrophysical Journal* 805.2, p. 156. DOI: [10.1088/0004-637X/805/2/156](https://doi.org/10.1088/0004-637X/805/2/156).
- Takahashi, K. et al. (2013). “Evolution of Progenitors for Electron Capture Supernovae”. In: *The Astrophysical Journal* 771.1, p. 28. DOI: [10.1088/0004-637X/771/1/28](https://doi.org/10.1088/0004-637X/771/1/28).
- Tang, J. et al. (2014). “New PARSEC evolutionary tracks of massive stars at low metallicity: testing canonical stellar evolution in nearby star-forming dwarf galaxies”. In: *Monthly Notices of the Royal Astronomical Society* 445.4, pp. 4287–4305. DOI: [10.1093/mnras/stu2029](https://doi.org/10.1093/mnras/stu2029).
- Tauris, T. M. and E. P. J. van den Heuvel (2006). “Formation and evolution of compact stellar X-ray sources”. In: *Compact stellar X-ray sources*. Vol. 39. Cambridge Astrophysics Series. Cambridge University Press, pp. 623–665.
- Tauris, T. M. et al. (2015). “Ultra-stripped supernovae: progenitors and fate”. In: *Monthly Notices of the Royal Astronomical Society* 451.2, pp. 2123–2144. DOI: [10.1093/mnras/stv990](https://doi.org/10.1093/mnras/stv990).
- Tauris, T. M. et al. (2017). “Formation of Double Neutron Star Systems”. In: *The Astrophysical Journal* 846.2, 170, p. 170. DOI: [10.3847/1538-4357/aa7e89](https://doi.org/10.3847/1538-4357/aa7e89).
- Timmes, F. X. et al. (1996). “The Neutron Star and Black Hole Initial Mass Function”. In: *The Astrophysical Journal* 457, p. 834. DOI: [10.1086/176778](https://doi.org/10.1086/176778).
- Tolman, Richard C. (1939). “Static Solutions of Einstein’s Field Equations for Spheres of Fluid”. In: *Physical Review* 55.4, pp. 364–373. DOI: [10.1103/PhysRev.55.364](https://doi.org/10.1103/PhysRev.55.364).
- Turolla, R. (2019). *Relativistic astrophysics*. Lecture notes. University of Padua.
- van den Heuvel, E. P. J. (2007). “Double Neutron Stars: Evidence For Two Different Neutron-Star Formation Mechanisms”. In: *The Multicolored Landscape of Compact Objects and Their Explosive Origins*. Vol. 924. AIP Conference Series, pp. 598–606. DOI: [10.1063/1.2774916](https://doi.org/10.1063/1.2774916).
- van Leeuwen, J. et al. (2015). “The Binary Companion of Young, Relativistic Pulsar J1906+0746”. In: *The Astrophysical Journal* 798.2, p. 118. DOI: [10.1088/0004-637X/798/2/118](https://doi.org/10.1088/0004-637X/798/2/118).
- Verbunt, F. (1993). “Origin and evolution of X-ray binaries and binary radio pulsars.” In: *Annual Review of Astronomy and Astrophysics* 31, pp. 93–127. DOI: [10.1146/annurev.aa.31.090193.000521](https://doi.org/10.1146/annurev.aa.31.090193.000521).
- Verbunt, F. et al. (2017). “The observed velocity distribution of young pulsars”. In: *Astronomy & Astrophysics* 608, A57, A57. DOI: [10.1051/0004-6361/201731518](https://doi.org/10.1051/0004-6361/201731518).
- Vigna-Gómez, A. et al. (2018). “On the formation history of Galactic double neutron stars”. In: *Monthly Notices of the Royal Astronomical Society* 481.3, pp. 4009–4029. DOI: [10.1093/mnras/sty2463](https://doi.org/10.1093/mnras/sty2463).
- Wald, R. M. (1984). *General relativity*. University of Chicago Press.
- Webbink, R. F. (1984). “Double white dwarfs as progenitors of R Coronae Borealis stars and type I supernovae.” In: *The Astrophysical Journal* 277, pp. 355–360. DOI: [10.1086/161701](https://doi.org/10.1086/161701).

- Webbink, R. F. (1985). “Stellar evolution and binaries”. In: *Interacting Binary Stars*. Ed. by J. E. Pringle and R. A. Wade. Cambridge Astrophysics Series. Cambridge University Press, p. 39.
- Wongwathanarat, A. et al. (2013). “Three-dimensional neutrino-driven supernovae: Neutron star kicks, spins, and asymmetric ejection of nucleosynthesis products”. In: *Astronomy & Astrophysics* 552, A126. DOI: [10.1051/0004-6361/201220636](https://doi.org/10.1051/0004-6361/201220636).
- Woosley, S. E. et al. (2002). “The evolution and explosion of massive stars”. In: *Reviews of Modern Physics* 74.4, pp. 1015–1071. DOI: [10.1103/RevModPhys.74.1015](https://doi.org/10.1103/RevModPhys.74.1015).
- Yakovlev, D. G. et al. (2013). “Lev Landau and the concept of neutron stars”. In: *Physics-Uspekhi* 56.3, pp. 289–295. DOI: [10.3367/ufne.0183.201303f.0307](https://doi.org/10.3367/ufne.0183.201303f.0307).
- Zahn, J. -P. (1975). “The dynamical tide in close binaries.” In: *Astronomy & Astrophysics* 41, pp. 329–344.
- (1977). “Tidal friction in close binary stars.” In: *Astronomy & Astrophysics* 500, pp. 121–132.
- Zee, A. (2013). *Einstein gravity in a nutshell*. Princeton University Press.

“ Today everybody is talking about virtual reality, but I think –frankly– that virtual reality is a rather miserable idea. It simply means: let us reproduce in an artificial digital medium our experience of reality.

I think that a much more interesting notion –crucial to understand what goes on today– is the opposite: not virtual reality, but the reality of the virtual. That is to say: reality –by this I mean efficacy, effectiveness, real effects– produced, generated by something which does not yet fully exists, which is not yet fully actual. ”

Slavoj Žižek
The Reality of the Virtual